

The population of SNe/SNRs in the starburst galaxy Arp 220

A self-consistent analysis of 20 years of VLBI monitoring

E. Varenius¹, J. E. Conway¹, F. Batejat¹, I. Martí-Vidal¹, M. A. Pérez-Torres^{2,3},
S. Aalto¹, A. Alberdi², C. J. Lonsdale⁵, and P. Diamond⁴

¹ Department of Earth and Space Sciences, Chalmers University of Technology Onsala Space Observatory, 439 92 Onsala, Sweden
e-mail: varenius@chalmers.se

² Instituto de Astrofísica de Andalucía (IAA, CSIC), Glorieta de las Astronomía, s/n, E-18008 Granada, Spain.

³ Departamento de Física Teórica, Facultad de Ciencias, Universidad de Zaragoza, Spain.

⁴ SKA Organisation, Jodrell Bank Observatory, Lower Withington, Macclesfield, Cheshire SK11 9DL, UK

⁵ Massachusetts Institute of Technology, Haystack Observatory, Westford, MA 01886, USA

Submitted to Astronomy & Astrophysics

ABSTRACT

Context. The nearby ultra-luminous infrared galaxy (ULIRG) Arp 220 is an excellent laboratory for studies of extreme astrophysical environments. For 20 years, Very Long Baseline Interferometry (VLBI) has been used to monitor a population of compact sources thought to be supernovae (SNe), supernova remnants (SNRs) and possibly active galactic nuclei (AGNs). SNe and SNRs are thought to be the sites of relativistic particle acceleration powering the star formation induced radio emission, and are hence important for studies of e.g. the origin of the FIR-radio correlation.

Aims. In this work we aim for a self-consistent analysis of a large collection of Arp 220 continuum VLBI data sets. With more data and improved consistency in calibration and imaging, we aim to detect more sources and improve source classifications with respect to previous studies. Furthermore, we aim to increase the number of sources with robust size estimates, to analyse the compact source luminosity function (LF), and to search for a luminosity-diameter (LD) relation within Arp 220.

Methods. Using new and archival VLBI data spanning 20 years, we obtain 23 high-resolution radio images of Arp 220 at wavelengths from 18 cm to 2 cm. From model-fitting to the images we obtain estimates of flux densities and sizes of all detected sources. The sources are classified in groups according to their observed lightcurves, spectra and sizes. We fit a multi-frequency supernova light-curve model to the object brightest at 6 cm to estimate explosion properties for this object.

Results. We detect radio continuum emission from 97 compact sources and present flux densities and sizes for all analysed observation epochs. The positions of the sources trace the star forming disks of the two nuclei known from lower-resolution studies. Multiple sources are found to expand with speeds of a few thousand km/s over a six year period. We find evidence for a LD-relation within Arp 220, with larger sources being less luminous. We find a compact source LF $n(L) \propto L^\beta$ with $\beta = -2.02 \pm 0.11$, similar to SNRs in normal galaxies. We find the observed size distribution to be bi-modal, indicating two distinct source populations. Based on simulations we argue that there are many relatively large and weak sources below our detection threshold. We show that the apparent short term variability reported by Batejat et al. (2012) for three sources can be explained in terms of convolution effects in regions with low surface brightness, rather than by intrinsic variability. Two sources are discussed in more detail: the brightest (at 6 cm) object 0.2195+0.492 is modelled as a radio SN with an unusually long 6 cm rise time of 17 years. The rapidly declining object 0.2227+0.482 is proposed as a possible AGN candidate.

Conclusions. The observations can be explained by a mixed population of SNe and SNRs, where the former expand in a dense circumstellar medium (CSM) and the latter interact with the surrounding interstellar medium (ISM). Several sources (9 of the 94 with fitted sizes) are likely luminous, type IIIn SNe. This number of luminous SNe correspond to few percent of the total number of SNe in Arp 220 which is consistent with a total SN-rate of 4 yr^{-1} as inferred from the total radio emission given a normal stellar initial mass function (IMF). Based on the fitted luminosity function, we argue that emission from all compact sources, also below our detection threshold, make up at most 20% of the total radio emission at GHz frequencies. However, colliding SN shocks and the production of secondary electrons through cosmic ray (CR) protons colliding with the dense ISM may cause weak sources to radiate much longer than assumed in this work. This could potentially explain the remaining fraction of the smooth synchrotron component. Future deeper observations of Arp 220 will probe the sources with lower luminosities and larger sizes. This will further constrain the evolution of SNe/SNRs in extreme environments and the presence of AGN activity.

Key words. Galaxies: star formation, starburst, individual: Arp 220 – ISM: supernova remnants – Stars: supernovae: general

1. Introduction

The ultra luminous infrared galaxy (ULIRG) Arp 220 (Arp 1966) is a merging system with two nuclei (east and west) about 1'' (370 pc) apart (Norris 1988). The nuclei are hosts of intense star formation (e.g. Parra et al. 2007) as well as possible AGN activity (Downes & Eckart 2007). Arp 220 has been subject of

global VLBI monitoring for 20 years, starting with the discovery of multiple compact ($<1\text{pc}$) sources by Smith et al. (1998b) at 18 cm. Subsequent observations revealed approximately 50 sources thought to be a radio SNe and/or SNRs, with many sources seen at multiple wavelengths (Rovilos et al. 2005; Lonsdale et al. 2006; Parra et al. 2007; Batejat et al. 2011, 2012).

Multiple sources in Arp 220 were resolved by Batejat et al. (2011) and shown to be consistent with an LD-relation of $L \propto D^{-9/4}$ when extrapolating from the lower density galaxies LMC and M82. The data presented by Batejat et al. (2011) were however not sensitive enough to determine an LD-relation within Arp 220 itself. Evidence for possible variability in three sources was presented by Batejat et al. (2012), but these sources are very weak, and multiple sensitive observing epochs are required to determine the nature of the apparent variability.

With its large population of SNe/SNRs in a very dense ISM ($\sim 10^5 \text{ cm}^{-3}$; Scoville et al. (2015)) with strong (mGauss) magnetic fields (Lacki & Beck 2013; Yoast-Hull et al. 2016), Arp 220 is an excellent laboratory to study the physics of star formation in extreme environments. The SNe/SNRs are also the sources of relativistic particles which are responsible for the star formation induced synchrotron radio emission in galaxies. Observational constraints on how SNe interact with a dense ISM may provide useful input to theories seeking to explain the well known FIR-radio correlation. Furthermore, the SNe blast waves are thought to be important for stellar feedback in galaxies, since they provide the driving force behind the large scale winds observed from dense starburst regions such as M 82.

The focus of this paper is to present a self-consistent set of data for the compact objects in Arp 220. We present both new and previously published data at multiple frequencies spanning 20 years. The new observations were designed to (1) improve our understanding of the evolutionary status of the SNe/SNRs, (2) investigate the LD-relation within Arp 220, (3) determine the nature of the variable sources. In addition to new data, archival data was re-analysed using similar calibration and imaging strategies to allow intercomparison. This paper presents the full data set and discusses the general properties of the population of compact objects. In future papers we intend to model in detail individual objects and the overall population of compact sources to constrain the evolutionary history of the compact radio objects.

This paper is organised as follows. In Sect. 2 we describe the observations as well as the method used to extract flux densities and sizes from the observed data. In Sect. 3 we present the results of our analysis. These results are discussed in Sect. 4 focusing on the statistical properties of the source population rather than individual objects. Finally, we summarise our conclusions and future work in Sect. 5.

Throughout this paper we assume an angular size distance to Arp 220 of 77 Mpc, i.e. $1 \text{ mas} = 0.37 \text{ pc}$, and luminosity distance of 80 Mpc, as obtained from Wright (2006) (with $H_0 = 69.9$, $\Omega_M = 0.286$ and $\Omega_{\text{vac}} = 0.714$) using $cz = 5469 \text{ km/s}$ (de Vaucouleurs et al. 1991)¹. All spectral indices α assume the flux density follows $S_\nu \propto \nu^{+\alpha}$.

2. Observations and data reduction

This paper presents data from 23 VLBI epochs at wavelengths from 18 to 2 cm, see Table 1, spanning 20 years. Nine of these data sets have not been published before. All data were processed into final images starting from the archival raw data. Most observations were performed with global VLBI using typically 15-20 antennas all over the world, including the VLBA and the EVN. The epochs GC031, BB297 and BB335 included multiple observations spanning a few months, the purpose being to look for short term variability. We note, however, that the epochs BB297B and BB297C were severely limited in sensitivity due to

Table 1. List of the 23 observations processed and analysed in this work. The RMS noise was measured in source free regions of the map.

Exp.	Obs. date YYYY-MM-DD	λ (cm)	Beam (mas)	Image RMS ($\mu\text{Jy}/\text{beam}$)
GL015	1994-11-13	18.1	8.2x2.5	33
GL021	1997-09-15	18.2	8.4x2.8	37
GL026	2002-11-16	18.2	6.4x2.9	11
GD017A	2003-11-09	18.2	6.7x2.8	10
GD017B	2005-03-06	18.2	6.2x3.1	14
BP129	2006-01-09	13.3	6.4x3.5	148
BP129	2006-01-09	6.0	2.7x1.4	87
BP129	2006-01-09	3.6	1.8x0.9	82
GD021A	2006-06-06	18.2	6.6x2.9	14
GC028	2006-11-28	3.6	1.4x0.5	35
GC028	2006-12-28	2.0	1.4x0.4	22
GC031A	2008-06-10	6.0	2.2x0.8	16
GC031B	2008-10-24	6.0	1.9x0.8	12
GC031C	2009-02-27	6.0	2.0x0.8	12
BB297A	2011-05-16	18.2	10.8x4.0	36
BB297A	2011-05-16	6.0	2.1x1.0	14
BB297A	2011-05-16	3.6	1.6x0.5	27
BB297B	2011-05-17	6.0	3.0x0.8	29
BB297C	2011-06-11	6.0	2.7x1.0	30
BB335A	2014-08-01	6.0	3.0x0.9	8
BB335A	2014-08-01	3.6	1.9x0.6	16
BB335B	2014-10-13	6.0	3.2x1.0	9
BB335B	2014-10-13	3.6	1.8x0.6	17

lack of fringes to multiple antennas, and therefore their respective 18 cm and 3.6 cm epochs (which are the least sensitive) have been excluded from the analysis in this paper.

All calibration and imaging was performed using the 31DEC16 release of the Astronomical Image Processing System (AIPS) (Greisen 2003) from the National Radio Astronomy Observatory (NRAO). The full reduction process, from loading of data to final images, was scripted for all data sets using the Python-based interface to AIPS, ParselTongue (Kettenis et al. 2006) 2.3. All the scripts are available via the CDS. A general description of the calibration strategy employed can be found in Appendix A. The interested reader may find all details, such as task parameters, in the ParselTongue scripts.

Previous studies of Arp 220 have used different (although similar) methods to analyse the data. For example, different criteria have been used to determine the catalogue of sources to analyse. In the following subsections we describe how we form a source catalogue, how we fit sizes and flux densities and estimate the corresponding uncertainties, and how we obtain more robust size-estimates by averaging measurements close in time.

2.1. Building a source catalogue

To increase our sensitivity for source detection we average all 6 cm images together, as a simple weighted average where each image was weighted by its sensitivity, given in Table 1, to the power of -2 .² By such averaging, we obtain the deepest maps

² We note that the images were averaged together without accounting for differences in respective synthesised beams. This should however only have a minor effect on finding the source positions to within $\pm 1 \text{ mas}$. However, for size measurements accounting for the effect of different beam shapes is important, as discussed in e.g. Sec. 3.3, and all sizes and flux densities in this work are measured from the single-epoch images.

¹ Via <http://vizier.u-strasbg.fr/viz-bin/VizieR?-source=VII%2F155>.

yet (off-source RMS noise $\sigma = 4.3 \mu\text{Jy}/\text{beam}$) of the two nuclei. The central parts of these two stacked images are presented in Fig. 1.

To produce a source catalogue we apply the source finding software PyBDSM version 1.8.6 (Mohan & Rafferty 2015) on the stacked image, with a threshold of six times the (stacked) image RMS noise, resulting in a catalogue of 75 sources at 6 cm. Similarly, we stacked the 18 cm and 3.6 cm images (stacked sensitivities of 5 and $10 \mu\text{Jy}/\text{beam}$ respectively) and detected 22 additional sources seen only at 18 cm (no new additions were found in the 3.6 cm images).³ The total catalogue hence contains 97 sources and is presented in Table 2. We note that three additional sources were detected in OH-maser emission only, i.e. no continuum, as briefly discussed in Appendix C.4.1. The maser channels in the data were however excluded when making the FITS images attached to this paper.

To estimate the expected number of false positives we use a beam of major and minor FWHM 3 mas and 1 mas respectively (similar to the most sensitive epochs which have the largest impact on the weighted average). Given the number of independent beam elements searched across the two nuclei, a threshold of 6σ implies an expected number of false positives of $6 \cdot 10^{-4}$, i.e. well below one. We note that lowering the threshold to 5σ would give one expected false detection.

2.2. Fitting source sizes and flux densities

In principle, it is best to fit models directly to the calibrated visibilities, instead of the cleaned images, to avoid any effects introduced by deconvolution (e.g. Martí-Vidal et al. 2014). However, the amount of data processed in this work make visibility fitting impractical. We therefore decided to fit models to the cleaned images. All sources were assumed to be optically thin shells with a fractional shell width of 30%, similar to the value observed for SN1993J (see e.g. Martí-Vidal et al. 2011b).⁴ The fitting was done using the bounded least-squares algorithm implemented in the Python package SciPy⁵. More details and examples of fitting results are presented in Appendix B. A comparison of the results obtained in this work with previous published values using the same data is presented in Appendix C. We note that although we fit sizes at all wavelengths, the angular resolution at 18 cm and 13 cm is not sufficient to obtain meaningful sizes at these wavelengths.

2.3. Uncertainties

Based on the observed scatter of the fitted positions (see Appendix C.2), we estimate that the catalogue positions given in Table 2 are accurate to within ± 1 mas. For flux densities we estimate the uncertainty as

$$E_f = \sqrt{(3\sigma)^2 + (0.1F)^2}$$

³ We note that 15 sources were only detected at 6 cm, but care should be taken when comparing frequencies given the different sensitivities. In particular, the spectral indices of the sources (affected by e.g. no, little or severe free-free absorption) combined with differences in luminosity may explain the differences in numbers at different frequencies.

⁴ We note that there may be ejecta opacity effects present in some sources, as well as asymmetrical structure. Such details are however beyond the scope of this work, and are the subject of a future, more detailed analysis.

⁵ Using the function `scipy.optimize.least_squares` which offers bounded fitting since early 2016.

where σ is the map RMS and F is the measured flux density. This includes both a conservative estimate of the image noise effects, as well as a 10% uncertainty on the absolute flux density calibration. Finally, for source sizes, we adopt an uncertainty based on Eq. 7 by Martí-Vidal et al. (2012) of

$$E_s = b_{\min} / \sqrt{STN} \quad (1)$$

where b_{\min} is the minor axis of the fitted CLEAN beam, and STN is the signal-to-noise ratio defined as F divided by the respective map RMS noise. We find the uncertainties calculated above to reflect well the observed scatter in the data.

2.4. Averaging of multiple epochs

Although we fit source flux densities and sizes at each epoch separately, the uncertainties are sometimes very large, in particular on the sizes of the weakest sources. We therefore, in some sections of this paper, calculate and discuss average sizes and flux densities using measurements from multiple epochs. An average size is calculated as the weighted average

$$\bar{s} = \frac{\sum s_i / E_{s_i}^2}{\sum 1 / E_{s_i}^2} \quad (2)$$

where the error on the weighted mean is calculated as

$$\bar{E}_s = \frac{1}{\sum 1 / E_{s_i}^2} \quad (3)$$

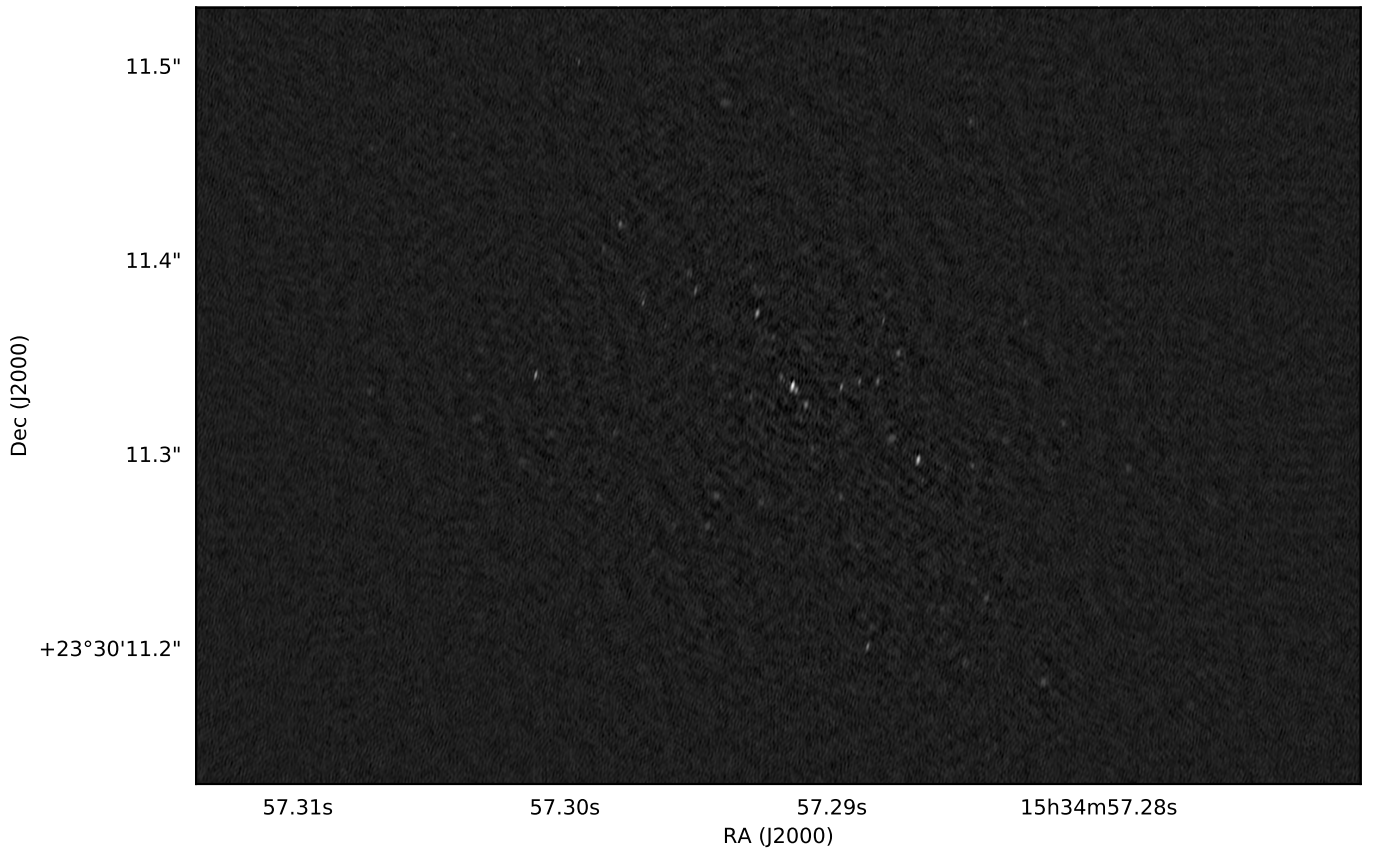
where s_i is a size fitted from an image and E_{s_i} is the corresponding uncertainty according to Eqn. 1. An average flux density is calculated in the same way, using the measured flux densities and their respective uncertainties instead of the sizes in Eqns. 2 and 3.

2.5. Source classification

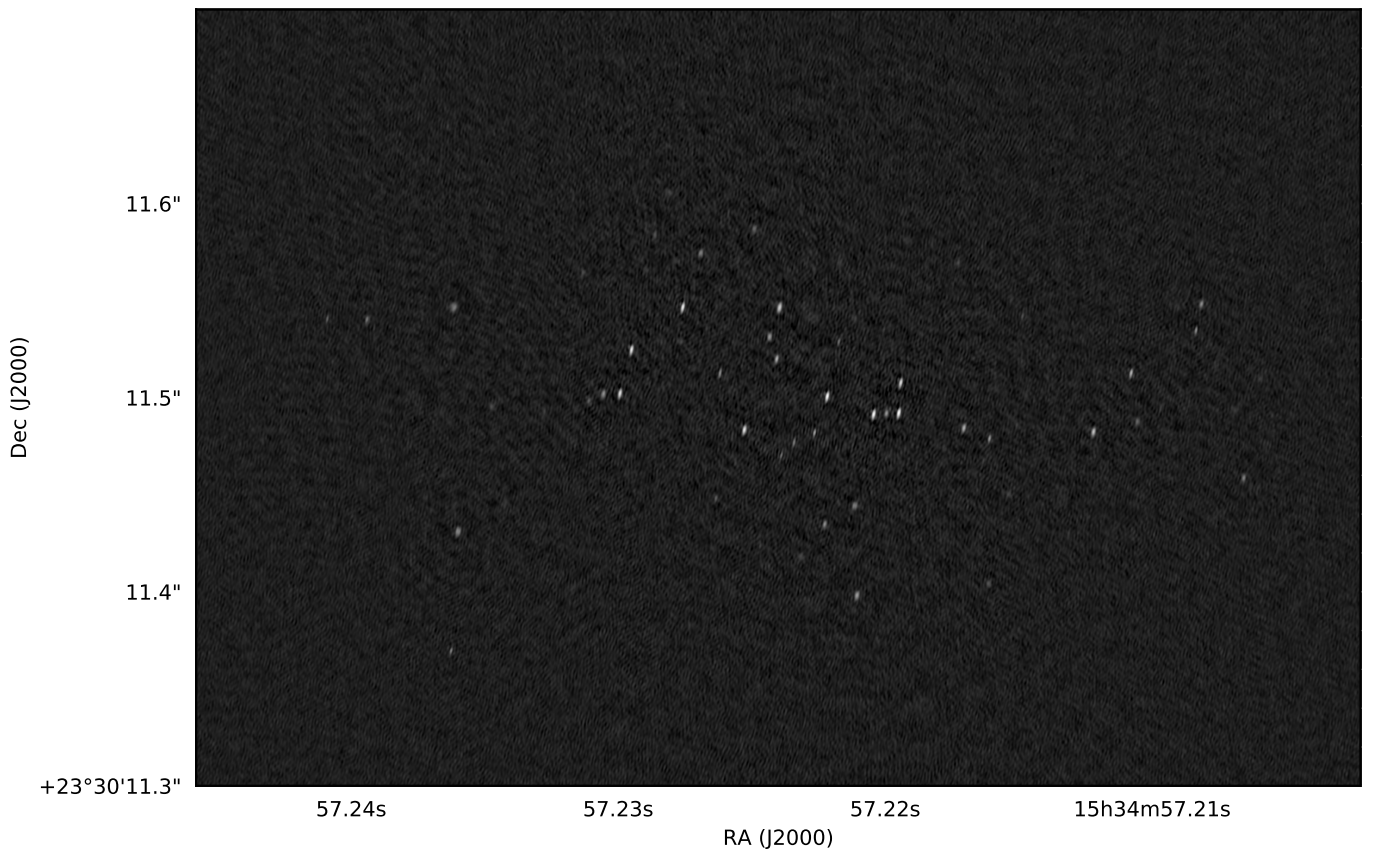
To facilitate a discussion of the data, we classified all sources in three groups based on their 6 cm evolution between the experiments GC031 and BB335. The sources were labelled either *Rise*, *Fall*, or *Slowly varying* (abbreviated S-var in many places in this paper) according to the following criteria. First, average flux densities and flux density uncertainties were calculated (as described in Sect. 2.4) for the GC031 and BB335 experiments, so that we obtained two flux density values per source. Let now F_{GC} and E_{GC} be the average flux density and flux density uncertainty for a given source obtained for the GC031 experiment, and F_{BB} and E_{BB} be the corresponding values for the BB335 experiment. A source was classified as *Rise* if $(F_{GC} + E_{GC}) < 0.9 \times (F_{BB} - E_{BB})$ and as *Fall* if $(F_{GC} - E_{GC}) > 1.1 \times (F_{BB} + E_{BB})$. If none of these conditions were satisfied, i.e. if there was no strong 6 cm evidence that a source was increasing or decreasing, the source was classified as *Slowly varying* with respect to the noise. We note that weak sources in the S-var category are not ruled out from increasing or decreasing by more than 10%, but there is no positive evidence for such variations given the measured uncertainties. Two sources were not detected in either GC031 or BB335 and are hence labelled *N/A* in Table 2.

2.5.1. Motivation

Note the classification presented in Sect. 2.5 is purely observational: it does not imply any particular source nature (such as



(a) The eastern nucleus of Arp 220



(b) The western nucleus of Arp 220

Fig. 1. Cutouts of the central parts of the stacked 6 cm images towards the east and west nuclei of Arp 220, with off-source RMS noise $\sigma = 4\mu\text{Jy beam}^{-1}$. The two panels are displayed using the same *arcsinh* grayscale from $-20\mu\text{Jy beam}^{-1}$ (-5σ) to $1140\mu\text{Jy beam}^{-1}$ (the maximum brightness value). The full $0.8192'' \times 0.8192''$ images of both nuclei were used for the source finding, as described in Sect. 2.1. The positions of the sources studied in this work is shown in Fig. 3.

SNe/SNRs). A detailed interpretation of the nature of the sources should of course use all the available information. One may therefore ask why we decided to base the classification only on the 6 cm lightcurves? There are multiple reasons for this choice.

The purpose of this classification is to facilitate the discussion. However, we find it instructive to divide the sources in groups already for the presentation of the results in Sect. 3. Given the number of sources and the high level of detail in these data, a physical classification (in contrast to this observational one) requires an extensive discussion to motivate the different possible classes. Such a discussion would be out of place before all the results are presented.

One may argue that if one devises classifications solely based on one waveband, one should use 18 cm since it spans the longest period in time. However, the 18 cm behaviour varies considerably between sources which have similar trends at 6 cm. Indeed, multiple studies (e.g. Smith et al. 1998a; Lonsdale et al. 2006; Varenius et al. 2016) argue that free-free absorption may significantly impact the flux densities measured at 1.4 GHz, which indicate that a classification based on 18 cm lightcurves may not reflect intrinsic source properties. Finally, the 18 cm observations do not have enough angular resolution to properly disentangle the emission of all sources, as a few sources are very close, thus mixing the lightcurves of blended sources.

In principle, also the 6 cm measurements may be affected by free-free absorption, and therefore one should use the 3.6 cm measurements to classify sources based on intrinsic properties. However, given the available data, we find the 6 cm observations to provide more robust lightcurves. The reason for this is twofold: first, the 6 cm observations are, in general, more sensitive than the 3.6 cm observations. Second, although the recent 3.6 cm observations in experiment BB335 reach a relatively high sensitivity, we lack an experiment with comparable sensitivity far back in time. At 6 cm we have the experiments GC031 and BB335, both with high sensitivity, separated by about 6 years in time. Given the above arguments, we decided to use the 6 cm lightcurves as the basis of our classification. We find that these simple classes provide an excellent foundation for the presentation of results and subsequent discussion of the data. We note that the physical nature of the sources is discussed in Sect. 4.

3. Results

We detect 97 compact continuum sources in Arp 220 with positions given in Table 2. The sources show a variety of lightcurves, spectra and sizes. A comprehensive summary of all data available for each source is presented in Appendix E. In this appendix, all measured flux densities and sizes are plotted as function of time for all sources. An approximate spectrum is also shown for each source. Note that all measured flux densities and sizes are also available in machine-readable format via CDS. The diameters and corresponding errors listed in Table 2 are calculated using Eqs. 2 and 3 from sizes fitted in the four images obtained at 6 cm and 3.6 cm in experiments BB335A and BB335B.

The sources were classified as described in Sect. 2.5. Examples of sources in the three categories *Rise*, *Fall*, and *Slowly varying* (or *S-var*) are shown in Fig. 2. For the purpose of the discussion we show two sources for each class to illustrate the variations in multifrequency lightcurves within the classes.

In Fig. 3, we show the positions of the sources, coloured by classification. The sources trace a region extended from east to west in the western nucleus, and from south-west to north-east in the eastern nucleus. This is consistent with the orientation of the

disks seen at lower spatial resolution at 5 GHz by Barcos-Munoz et al. (2015).

3.1. The luminosity-diameter relation

Fig. 4 shows the 6 cm spectral luminosity versus source diameter for the sources detected in Arp 220, i.e. the values listed in Table 2. The luminosities were calculated from the flux densities measured in BB335B while the sizes were averaged over the BB335 6 cm and 3.6 cm observations as described in Sect. 2.4. In Fig. 4b the data are shown in log-log scale together with 45 SNRs observed in the nearby galaxy M82, using data from Huang et al. (1994). We note that the two brightest SNRs in M82 overlap the weakest objects detected in Arp 220. For discussion purposes, we have also overlaid the evolution of the bright radio supernova SN1986J⁶ during its first 30 years, using the lightcurve model given by Weiler et al. (2002) together with the size evolution after t years of $D[\text{mas}] = 0.86 \cdot t^{0.71}$ and distance of 10 Mpc as given by Bietenholz et al. (2002).

The sources with BB335B 6 cm luminosities above $0.5 \times 10^{28} \text{ erg s}^{-1} \text{ Hz}^{-1}$ are all consistent with reaching 6 cm peak luminosities of about $10^{28} \text{ erg s}^{-1} \text{ Hz}^{-1}$ during their evolution, see the lightcurves in appendix E. From Fig. 4 we note that most *rising* sources are relatively small ($D < 0.4 \text{ pc}$). Given their current lightcurves, some of the weaker rising sources are unlikely to reach 6 cm peak luminosities of $\sim 10^{28} \text{ erg s}^{-1} \text{ Hz}^{-1}$, e.g. 0.2084+0.534, while others e.g. 0.3011+0.341 may reach these luminosities in a few years time.

The *slowly varying* sources occupy all regions of Fig. 4. They are all consistent with either being near their 6 cm peak luminosity, or in a state of slow decline. Some of these sources have slowly varying 18 cm lightcurves, e.g. Fig. 2c, while others show rapidly changing 18 cm lightcurves, e.g. Fig. 2d. Some are optically thin (e.g. $L_{18 \text{ cm}} > L_{6 \text{ cm}} > L_{3.6 \text{ cm}}$) while others show almost no 18 cm emission while still clearly detected in multiple epochs at shorter wavelengths.

The *falling* sources also occupy all regions of Fig. 4. Some of these, e.g. 0.2227+0.482, show relatively rapid (50% in 10 years) optically thick decline from a peak luminosity of $> 10^{28} \text{ erg s}^{-1} \text{ Hz}^{-1}$ without any clear 18 cm detection. Others, e.g. 0.2122+0.482, show an optically thin decline with prominent 18 cm emission since 1994.

3.2. Source expansion from 2008 to 2014?

Given that we have data spanning many years one could try to measure if sources are expanding between the observing epochs. However, an expansion speed of $< 10000 \text{ km/s}$, as expected for the SNe in Arp 220 (Batejat et al. 2011), translates to an increase in diameter of $< 0.02 \text{ pc}$ in one year. Even using the most sensitive 6 cm data, such a small increase is very challenging to detect between two single epochs given the uncertainties on our size measurements.

To reduce uncertainties we average the sizes (as described in Sect. 2.4) for the most sensitive series of 6 cm epochs close in time, i.e. the epochs within experiments GC031 and BB335, to obtain more robust size measurements separated by about 6

⁶ SN1986J was chosen because it is the highest luminosity radio SNe ($L_{6 \text{ cm}}^{\text{peak}} = 1.97 \times 10^{28} \text{ erg s}^{-1} \text{ Hz}^{-1}$; Weiler et al. (2002)) to have good VLBI size measurements. Sources with higher peak luminosity have been observed (e.g. SN1988Z; Weiler et al. (2002)) but these are significantly more distant and hence both weaker and smaller in angular size.

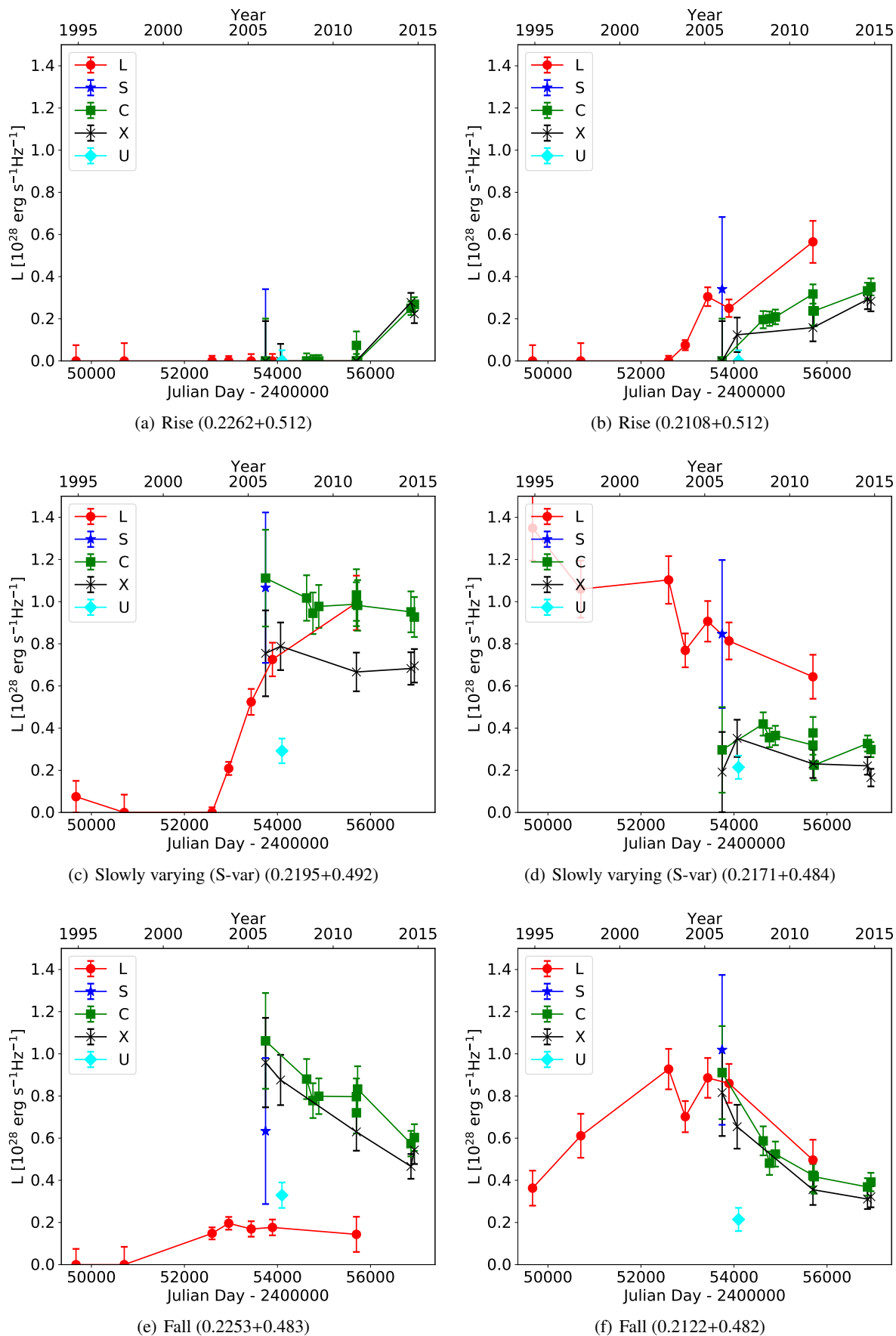


Fig. 2. Lightcurves to illustrate the source classifications *Rise*, *Slowly varying* (or *S-var*) and *Fall* used in this paper. For the purpose of the discussion, two sources are shown for each class, to show the differences in multifrequency behaviour within the classes. All panels have the same scale for easy comparison. The horizontal axis below the panels show time in Julian Days, while the horizontal axis on top of the panels show the time in decimal years. In Sect. 4.3 we argue that these lightcurves are consistent with SNe/SNRs in different evolutionary stages, where the approximate time scale corresponds to panels a, c, f, b, d. Panel e may represent a stage similar to f but with significant free-free absorption.

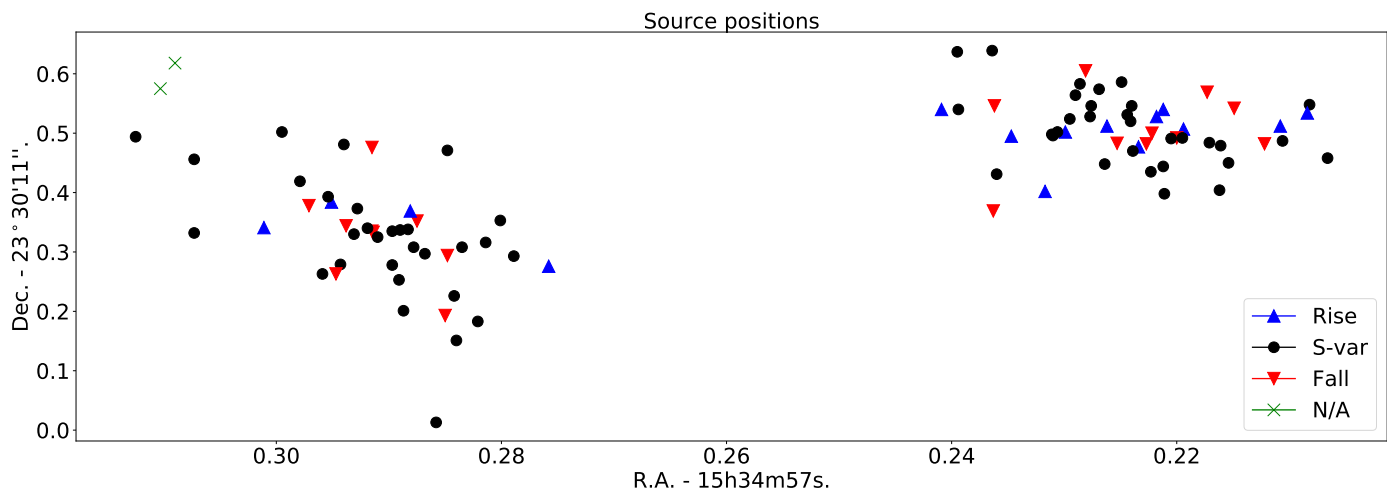


Fig. 3. The spatial distribution of all sources given in Table 2 with the eastern nucleus to the left and the western nucleus to the right. Each source is coloured by its observational classification, as described in Sect. 3. Note that a few sources are detected in the eastern nucleus outside the central cutout region shown in Fig. 1a.

years in time. The new diameters (BB335) versus the old diameters (GC031) are shown in Fig. 5. Despite significant scatter and large uncertainties, there seems to be a trend of expansion for sources smaller than about 0.6 pc. i.e. most sources are above the solid line which marks no change. The measured speeds of a few thousand km/s are consistent with SN shocks.

For the larger sources the lack of expansion, or even apparent shrinking larger than the formal error bars, can be explained by differences in sensitivity where the fitted size may vary because of the low emitted surface brightness combined with noise and beam effects, as discussed in Sect. 3.3. Also, older sources are expected to decelerate as well as fade, making any expansion harder to detect.

3.3. Weak large sources can appear variable

Batejat et al. (2012) discussed three sources possibly varying in position, shape and flux density: $0.2212+0.444$ (W29), $0.2223+0.435$ (W26), and $0.2362+0.546$ (W7). While these sources have been observed for many years, they appeared to vary on the timescale of months, based on imaging of the three GC031-epochs. Various explanations were proposed as AGN activity, microblazars, and SNR shell variability.

We note that the apparent variability is however always along the minor axis of the beam, see Batejat et al. (2012), their Fig. 2. In all three GC031-epochs the synthesised beam is elongated south-east to north-west (position angle about -15°). A weak circularly symmetric ring-like structure convolved with such an elongated beam would appear as a double source with position angle -15° . For a large (clearly resolved) SNR, we expect to detect the north-east and south-west parts more easily than the north-west and south-east parts, even if the shell is spherically symmetric. For a weak SNR, with surface brightness comparable to the image noise, the noise may affect the observed emission from the shell and thereby cause apparent variability very similar to the changes reported by Batejat et al. (2012).

We simulated this effect by modelling a shell of diameter 0.8 pc with flux density 0.4 mJy, and relative shell width of 30%. The model was convolved with the clean restoring beam of each GC031-epoch, and noise was added from three arbitrary source-free positions in the corresponding VLBI image of the western nucleus. Our simulations show variability in position, shape and

flux density, see Fig. 6, in close agreement with what was observed by Batejat et al. (2012). We also see similar apparent variability in later 6 cm images of these three sources, although less in the most sensitive BB335-epochs as expected when the signal-to-noise is higher. Finally, we also, as expected, detect more sources with similar behaviour in our recent high-sensitivity 6 cm observations, for example $0.2249+0.586$, $0.2269+0.574$, and $0.2360+0.431$.

Given the above results we propose that the three sources discussed by Batejat et al. (2012) are in fact large SNRs, and that the apparent variability is caused by combined effects of image noise and surface brightness sensitivity due to the shape of the synthesised beam. Using the model-fitting approach described in Sect. 2.2, we have obtained relatively large (0.9, 0.6, 1.1 pc respectively) sizes for all three objects ($0.2212+0.444$, $0.2223+0.435$, $0.2362+0.546$), consistent with the SNR hypothesis.

3.4. The measured distribution of source diameters

The measured source sizes are shown as a histogram in Fig. 7, i.e. a projection of Fig. 4 onto the horizontal axis. The size distribution appears double humped, with peaks around 0.25 pc and 0.8 pc, and falls off around a diameter of 1 pc. The shape of the distribution can be explained as two underlying distributions truncated by the observational limits in surface brightness. The underlying distributions are discussed further in Sect. 4.

Weak sources with surface brightness near our detection limit (dashed line in Fig. 4) may appear both smaller and larger than their actual size, see also appendix D and Sect. 3.3. This effect means that we expect to measure the wrong sizes for a few objects. It is hard to quantify how these effects affect the measured size distribution, but we believe the combination of a lack of detections of some large sources together with some weak sources being fitted as smaller than their real size does contribute to the shape of Fig. 7.

3.5. The source luminosity function

It is clear from Fig. 4 that there are relatively few strong sources. However, while the high-luminosity sources are all relatively small in size, the lower-luminosity sources are a mixture of large and apparently small sources. A large fraction of the small and

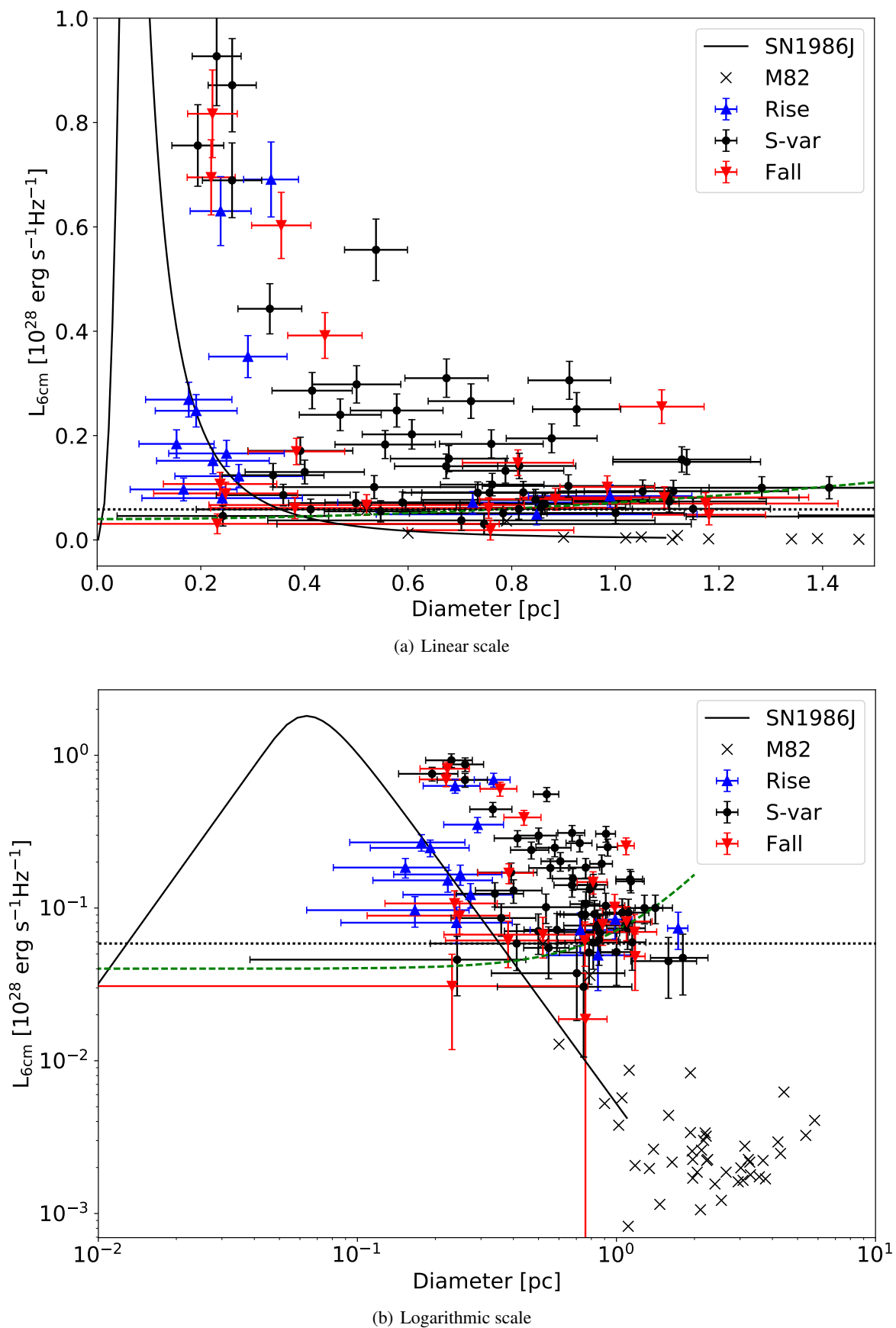


Fig. 4. The data in Table 2 plotted as luminosity vs diameter in linear scale (panel a) and log scale (panel b). The surface brightness detection limit of BB335B is shown as a dashed line, and the fitted luminosity completeness limit L_c , as derived in Sect. 3.5, is shown as a dotted line. The lower panel show 45 SNRs in M 82 plotted as black crosses (data from Huang et al. 1994, their Table 2, scaled to 6 cm assuming $\alpha = -0.5$). The evolution of SN1986J during the first 30 years is plotted as a solid curve, from the model described in Sect. 3.1.

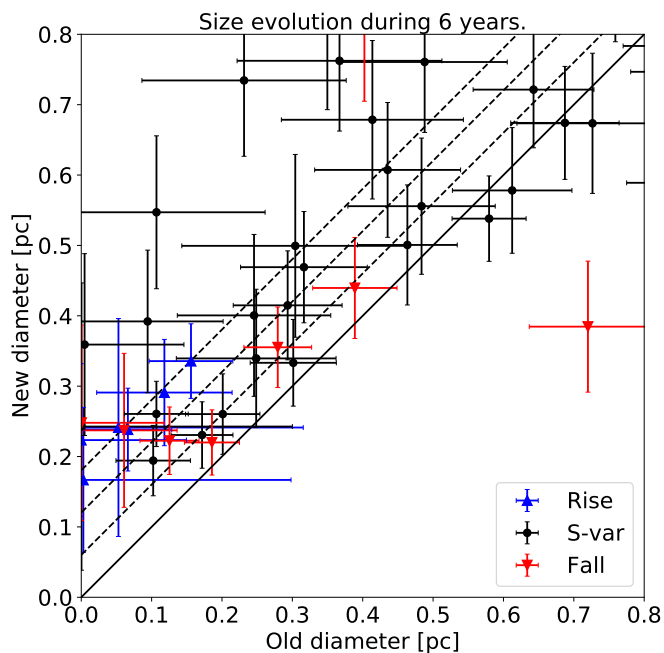


Fig. 5. Size evolution at 6 cm from epochs GC031 (horizontal axis) to BB335 (vertical axis) Sources larger than 0.6 pc are too weak to obtain robust estimates of expansion velocities. The three dashed lines mark expansion velocities of 5000km/s, 10000km/s and 15000km/s. Despite significant scatter and large uncertainties, sources smaller than 0.6 pc are consistent with expansion speeds of a few thousand km/s.

weak sources may appear smaller than their actual sizes as discussed in the previous section. However, simulations show, see appendix D, that this scattering of sizes has little effect on the measured luminosities. Thus the sampled luminosity function, shown as a histogram in Fig. 8 and as a cumulative function in Fig. 9, should be a good measure of the true luminosity function.

Chomiuk & Wilcots (2009) investigate the SNR LF in 18 “normal” galaxies at 1.45 GHz by fitting the power law

$$n(L) = AL_{24}^{\beta} \quad (4)$$

where A is a scaling factor (accounting for e.g. SFR), β is a negative number (predicted by Chomiuk & Wilcots (2009) to be -2.1) and L_{24} is the 1.45 GHz luminosity given in units of $10^{24} \text{ erg s}^{-1} \text{ Hz}^{-1}$. Using maximum likelihood estimation methods (MLE) Chomiuk & Wilcots (2009) find a slope $\beta = -2.07 \pm 0.07$ from combining 258 SNRs in all 18 galaxies, in very good agreement with the predicted value.

In addition to the 18 galaxies, Chomiuk & Wilcots (2009) investigate the LF in Arp 220 using eight SNRs listed by Parra et al. (2007). They find $\beta = -3.00 \pm 1.89$ which, although consistent with the predicted value, suffers severely from small sample statistics.

We analyse the Arp 220 LF as sampled by the 91 sources detected at 5 GHz in experiment BB335B. Assuming an average spectral index of $\alpha = -0.5$ (as modelled by Chomiuk & Wilcots (2009) assuming the CR electron energy spectrum can be described as a power law E^{-2}), we extrapolate the flux densities measured at 5 GHz (given in Table 2) to 1.45 GHz for direct comparison with Chomiuk & Wilcots (2009). We note that this extrapolation likely gives a better estimate of the intrinsic 1.45 GHz emission than directly using values measured at closer frequencies because of the significant free-free absorption affecting the radio emission from Arp 220 below 2 GHz (Smith et al. 1998a; Lonsdale et al. 2006; Varenius et al. 2016).

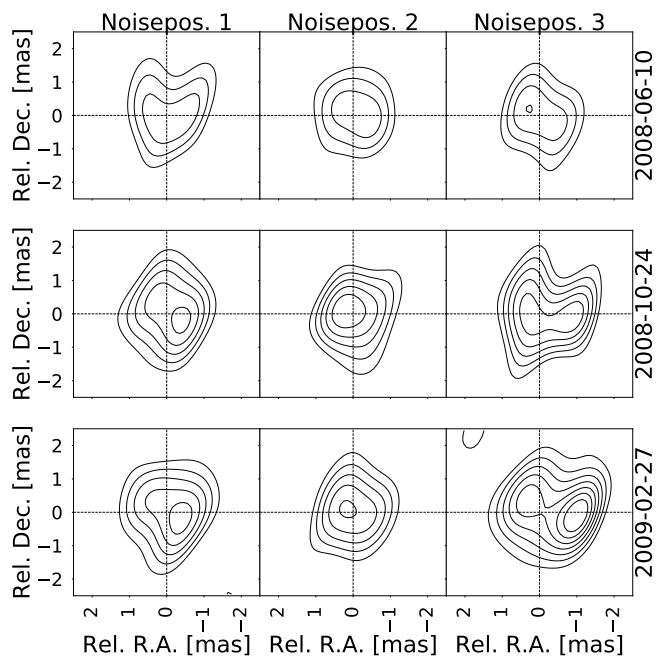


Fig. 6. Simulation of an optically thin shell of 0.4 mJy ($2.84 \cdot 10^{27} \text{ erg s}^{-1} \text{ Hz}^{-1}$) with diameter 2.2 mas (0.8 pc) using image noise and clean restoring beam from the three GC031-epochs. Contours at $(4,6,8,\dots) \times \sigma$. Noise have been extracted from three different (source-free) positions in the images (same position in each column in this figure). Even though the source model is the same in all the nine panels, we see clear apparent variability between the epochs (within each column) but also with respect to different noise positions in the same epoch (within each row). Compare to Batejat et al. (2012), their Fig. 2.

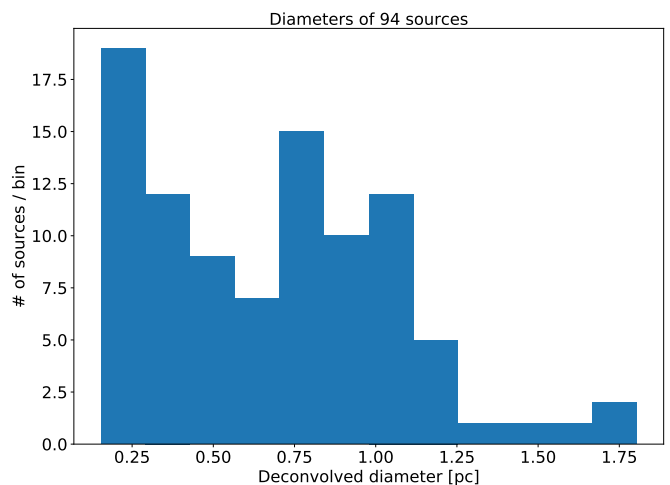


Fig. 7. The distribution of measured source diameters appears bi-modal, with peaks around 0.25 pc and 0.8 pc. We note that three of the 97 sources have no size estimates in either BB335A or BB335B and are therefore not included in this figure.

To determine β in Eq.4 we use the MLE methods of Clauset et al. (2009), i.e. the same as used by Chomiuk & Wilcots (2009), as implemented in the Python package *powerlaw* by Alstott et al. (2014). This enables determination of a completeness limit, i.e. the luminosity where the powerlaw turns over due to e.g. incomplete sampling of faint sources. The limit is found by creating a power-law starting from each unique value in the data set, then selecting the one that results in the minimal Kolmogorov-Smirnov distance between the data and the fit (see also the Ap-

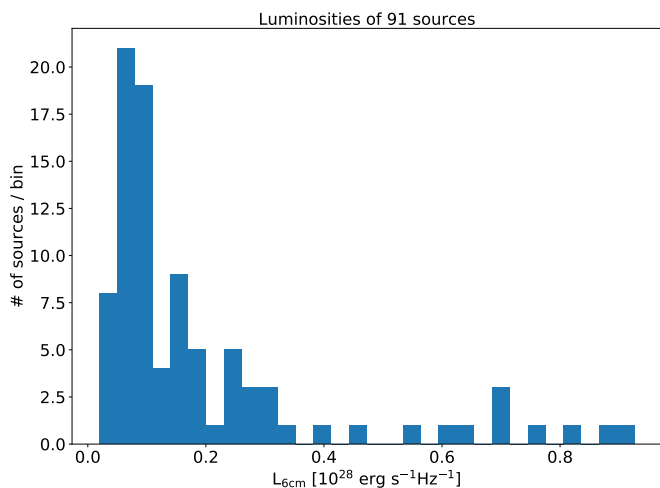


Fig. 8. The distribution of measured source luminosities, as measured in the epoch BB335B. Six of the 97 sources were not detected in this epoch, and have therefore been excluded from this figure.

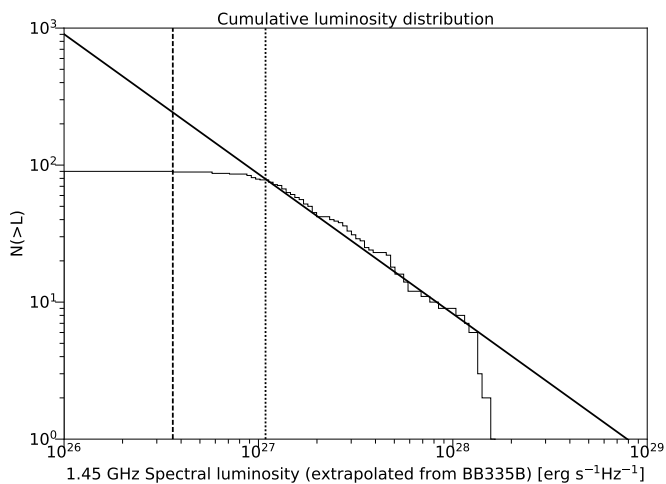


Fig. 9. The cumulative luminosity function for the 91 sources detected in BB335 (of the total 97 sources detected in all epochs). To be directly comparable with Chomiuk & Wilcots 2009, their Fig. 1, the luminosities have been extrapolated from Table 2 to 1.45 GHz, assuming a spectral index of -0.5 . A power-law fit is shown as a solid line. The point source detection limit is shown as a vertical black dashed line to the left, and fitted completeness limit (where the power law turns over) is shown as a dotted line.

pendix by Chomiuk & Wilcots 2009). We note that this limit is significantly higher than the point source detection threshold, see Fig. 9.

Using the 79 sources above our completeness limit (at 1.45 GHz) of $L_c = 1.09 \cdot 10^{27} \text{ erg s}^{-1} \text{ Hz}^{-1}$ we fit a slope $\beta = -2.02 \pm 0.11$ for Arp 220, in good agreement with the -2.1 predicted by Chomiuk & Wilcots (2009). We note that some sources in our sample (in particular those labelled *rising*) may not yet have reached the SNR stage. However, these are relatively few and excluding those 15 sources from the fit only changes the slope very marginally well within the given uncertainty (to $\beta = -2.04 \pm 0.13$).

The observed cumulative luminosity function as well as the best fit of Eq. 4 is shown in Fig. 9 along with the 3σ point source detection limit (in the BB335B epoch, i.e. a level similar to the 6σ limit used in the stacked map) and the fitted completeness limit L_c . The fact that the completeness limit is significantly

above the point source detection limit is not unexpected. Sources at, or below, the limit have resolved sizes so their luminosities are spread over multiple beam areas. Hence, in each beam area they would fall below the point source detection limit. We note that the fitted completeness limit could be a real lower limit to the SNR LF in Arp 220 and not just an observational effect, although this seems unlikely given that the turnover occurs close to where it is expected given that most weak sources are resolved.

By integration of Eq. 4 we obtain an expression for the number of sources above a certain luminosity as

$$N(L > L_{\min}) = \int_{L_{\min}}^{\infty} n(L) dL = -A \frac{L_{\min}^{\beta+1}}{\beta+1}. \quad (5)$$

Knowing that $N(L > L_c) = 79$, this expression can be used to estimate a value for A . Even though the parameter β is assumed to have Gaussian probability distribution (using MLE methods), the distribution of A is clearly asymmetric because of the exponential dependence on β . We determine A using a Monte-Carlo approach where we sample its distribution using 100,000 random draws of β from a Gaussian distribution with mean -2.02 and standard deviation 0.11 . From the resulting distribution of A -values we fit the cumulative distribution function using the interpolation approach implemented in the package *SciPy*⁷ to obtain three empirical quantiles corresponding to the -1σ , mean, and $+1\sigma$ values for a Gaussian distribution. From this we obtain a robust estimate of $A = 100,000^{+149,000}_{-60,000}$ where the uncertainty reflects the uncertainty in β . We note that this numeric value of A assumes a luminosity given in units of $10^{24} \text{ erg s}^{-1} \text{ Hz}^{-1}$ in Eq. 4. We also note that if we instead sample β from a Gaussian distribution with mean -2.07 and standard deviation 0.07 , i.e. the average value found by Chomiuk & Wilcots (2009), we obtain $A = 150,000^{+111,000}_{-64,000}$, in agreement with the value $A = 57,000^{+39,000}_{-19,000}$ obtained by Chomiuk & Wilcots (2009). Finally we note that if we fix $\beta = -2.1$ we obtain $A = 190,000$.

4. Discussion

As argued by previous studies, e.g. Parra et al. (2007), we expect a large ($\sim 4 \text{ yr}^{-1}$) rate of supernovae in Arp 220, of which only the most radio luminous objects are bright enough to be observed. Detailed studies of the radio emission from these radio luminous SNe in Arp 220 may allow us to constrain the properties of their CSM, and thus e.g. the mass loss histories of the progenitor stars. However, a detailed discussion of the evolution of each individual object is currently very challenging, given the complexity of SN evolution and the limited time range sampled by the observations at wavelengths shorter than 18 cm, and is therefore deferred to a future paper. In this section we discuss the radio emission following SN explosions, focusing on general properties of the population of compact sources.

4.1. The radio SN/SNR dichotomy

The evolution the radio emission arising after supernova explosions is often split in a radio SN-stage, where the blast wave is thought to interact primarily with the CSM, and a SNR-stage, where the blast wave interacts with the surrounding ISM. The passage of SN to SNR phase occurs when the supernova blast wave reaches the radius where the pressure of the ISM is approximately equal to the ram pressure of the wind. This is expected to happen earlier for SNe exploding in the high-pressure

⁷ Using the function `scipy.stats.mstats.mquantiles`.

environments of starbursts than in normal galaxies. We note that although this dichotomy is useful in many cases, it is an oversimplification of a broad range of possible evolutionary paths, depending on e.g. the progenitor mass loss history (i.e. CSM structure), the explosion geometry, the progenitor nature (single/binary), the structure and density of the surrounding ISM, and the magnetic fields in the CSM and ISM (see e.g. Weiler et al. 2002; Vink 2012; Dubner & Giacani 2015 and references therein). However, as a detailed discussion of the nature of individual objects is planned for a later paper, for the purpose of this discussion we adopt these simple labels of SNe for objects interacting primarily with their CSM, and SNRs for objects interacting primarily with the surrounding ISM.

4.2. Radio emission from SNe and SNRs

The intensity of radio emission from core-collapse SNe versus time is closely related to the density profile versus radius in the CSM. This relationship is complicated because of the presence of HII-regions and wind-blown bubbles which may have formed around the progenitor stars before the explosion. The structure of the CSM may be complex with e.g. layers having different densities and temperatures depending on the wind history of the progenitor (e.g. Weiler et al. (2002); Vink (2012)). Core-collapse SNe may show prominent emission within a few days after the explosion (e.g. SN1993J; Martí-Vidal et al. 2011b). In other cases it can take years for the radio emission to appear.

The observed radio emission is thought to come from a region right behind the SN blast wave, where charged particles are accelerated to relativistic energies and trapped in strong magnetic fields (Weiler et al. 2002). If the SN explodes in a low density CSM, very little radio emission is expected until the blast wave reaches the surrounding ISM. If, on the other hand, the SN explodes in a relatively high density CSM, the SN is expected to show a characteristic radio lightcurve, with the peak appearing later at longer wavelengths due to the free-free absorption by the ionised CSM (Weiler et al. 2002).

In a simple model, the radio emission is expected to increase (again) when the shock reaches the dense ISM (i.e. the SNR phase) and particle acceleration becomes efficient. The maximum luminosity during this phase is expected to occur at the *Sedov* radius, where the mass swept up by the blast wave is equal to the mass of the SN ejecta and the energy in relativistic electron reaches a maximum.

In the case of a very dense progenitor wind, i.e. a dense CSM, it is possible that the *Sedov* radius is reached already before the shock enters the ISM. For such objects there may not be a clear distinction between the SNe and SNR phases. Such dense wind progenitors are however expected to be rare, and the majority of SNe explosions in Arp 220 will likely produce weak and undetectable radio emission in the initial CSM phase and the sources will rise to a peak radio emission only when they begin interacting with the ISM.

4.3. The nature of the compact objects in Arp 220

Although most radio SNe may be relatively weak and hence below our detection limit, some may brighten enough to be detected when they reach the ISM. In addition to these SNRs (i.e. shocks interacting with the ISM), we expect to see the most luminous SNe which interact strongly with their dense CSM, such as type II_n (Chevalier et al. 2006; Petropoulou et al. 2016). This class of SNe is however thought to be rare and likely make up

only a few percent of the total SN population (Smith et al. 2011; Eldridge et al. 2013).

4.3.1. The nature of the brightest objects

The brightest objects in Fig. 4 all show lightcurves (see Appendix E) consistent with expansion in a dense, ionised CSM. Indeed, given the tentative expansion velocities of a few thousand km/s (Fig. 5) and their high luminosities, multiple objects are consistent with significantly longer rise times than expected if synchrotron self-absorption is the dominant absorption mechanism (Chevalier et al. 2006, their Fig. 2). It is thus likely that free-free absorption from the ionised CSM is significant in these objects.

Given the background presented in Sect. 4.2 we expect to see a few objects in the early radio SN-stage, rising at 3.6 and 6 cm but with weak or undetected 18 cm emission, such as 0.2262+0.512 (see Fig. 2a). Objects with high explosion energies evolving in a dense, ionised CSM are then expected to reach their respective peak luminosities later at longer wavelengths, such as 0.2195+0.492 (see Fig. 2c), followed by an optically thin decline such as 0.2122+0.482 (see Fig. 2f). As the shock wave reaches the ISM, the lightcurves may, in case of a sharp boundary to a higher-density ISM, rise at all frequencies, such as 0.2108+0.512 (see Fig. 2b) or, in case of no sharp boundary, flatten (as seems to be the case for 0.2122+0.482 in 2014) due to the constant density. The subsequent SNR phase, when the blast wave expands in the constant density ISM, is expected to show a slow optically thin decline, such as observed in 0.2171+0.484 (see Fig. 2d). Because multiple studies (e.g. Smith et al. 1998a; Lonsdale et al. 2006; Varenius et al. 2016) argue that (foreground) free-free absorption may significantly reduce the measured 18 cm flux densities, we expect to see a few sources, in particular towards the centres of the nuclei, with relatively weak 18 cm emission. This could explain the almost flat spectrum of 0.2122+0.482. Also 0.2253+0.483 (see Fig. 2e) could be an example of a blast wave hidden behind significant foreground absorption.

4.3.2. Modelling the lightcurves of the brightest object

It is challenging to derive accurate age estimates from the observed lightcurves, mainly because of the limited time coverage at 5 GHz and higher frequencies. Based on the lightcurves the brightest sources are, in general, likely a few decades old with 6 cm rise times of a few years. One way to estimate the age of the brightest sources is to use model-fitting of the lightcurve for a typical object. As an example, we choose the brightest object 0.2195+0.492, given that this object has the highest signal-to-noise and therefore should be the first candidate for model fitting from a data quality point of view. We used a simplified version of the model presented by Weiler et al. (2002), i.e. following the model described by Chevalier (1982a,b) where the radial density profile of the CSM is assumed to be $\propto r^{-2}$, as described by Eqns. 1 and 2 of Marchili et al. (2010). The best-fit parameters are $\alpha = -0.91$, $K_1=286$ Jy, $K_2 = 3.6 \times 10^9$, $\beta = -1.31$, and an explosion date of 1981-04-14 i.e. an observed age estimate (in BB335) of about 34 years, and a corresponding 6 cm peak time of about 17 years. This is significantly longer than the 1210 days listed as the longest rise-time in Weiler et al. (2002) (for SN1986J). The model is shown together with the data in Fig. 10. The fitted values imply a deceleration parameter $m = 0.87$ (from Eq. 7 by Weiler et al. 2002) and a pre-supernova mass-loss rate of

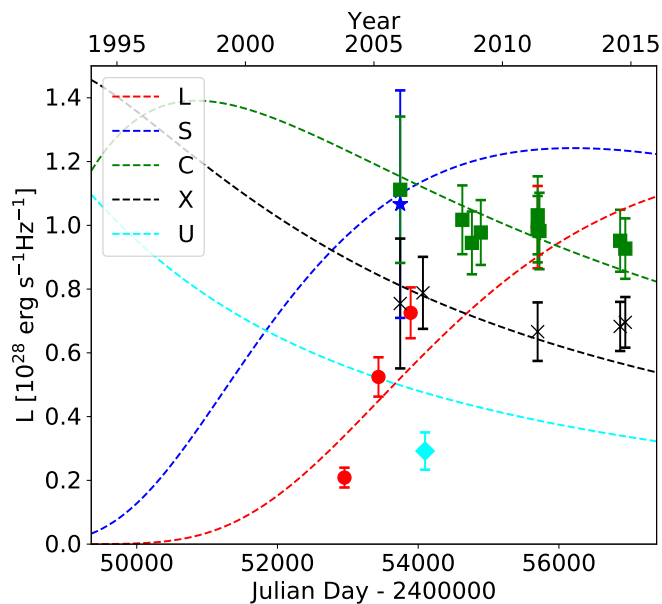


Fig. 10. The best-fit lightcurve model described in Sec. 4.3.2 overplotted on the observed detections of 0.2195+0.492.

$5 \times 10^{-7} M_{\odot} \text{yr}^{-1}$), assuming a wind speed of 10 km/s for a type II SN (Weiler et al. 2002; Eq. 18). We note that the estimated mass-loss rate is two orders of magnitude lower than for SN1986J, although this calculation is subject to many assumptions and the actual value may be much higher (Weiler et al. 2002). Given the age (and relatively modest deceleration) obtained and the measured diameter of 0.2195+0.492 of about 0.2 pc, a linear estimate implies an expansion velocity of ~ 3500 km/s, consistent with the expansion measured between the GC031 and BB335 epochs (see Fig. 5).

4.3.3. The observed number of luminous SNe

In Sect. 4.3.2 the brightest object is estimated to be about 30 years old. The lightcurves of other objects with similar current luminosity and size indicate a similar evolutionary history. If we, to increase statistics, select as luminous SNe the nine objects with $L_{6\text{cm}} > 0.5 \times 10^{28} \text{ erg s}^{-1} \text{ Hz}^{-1}$ and diameter < 0.4 pc, and assume these are at most 50 years old, this would correspond to an observed rate of the most luminous SNe of $\sim 0.2 \text{ yr}^{-1}$.

Given the total star formation rate of Arp 220 of $230 M_{\odot} \text{yr}^{-1}$ (Varenius et al. 2016) and using Eq. 2 in Smith et al. (1998b), assuming the same $m_l = 1 M_{\odot}$, $m_u = 45 M_{\odot}$ and $m_{\text{sn}} = 8 M_{\odot}$, we estimate a total SN-rate of about 4 yr^{-1} . If 5% (average of Smith et al. (2011); Eldridge et al. (2013)) of these end up as type II in during 50 years of continuous star formation, we expect to see 10 such objects, or a rate of luminous SNe of 0.2 yr^{-1} , i.e. in excellent agreement with the observed number. This suggests that a standard IMF in Arp 220 can explain the number of bright SNe observed in Arp 220.

We stress that both the measured and expected value likely suffer from small number statistics, where e.g. a few of the small rising sources may rise above $5 \times 10^{28} \text{ erg s}^{-1} \text{ Hz}^{-1}$ within a few years. Furthermore, we may, given the sparse sampling in time, miss some very rapidly evolving SN of types Ib/c, which could be luminous enough to be seen about our detection threshold but rising and falling between the observations. Finally, our SN-rate estimate are subject to uncertainties related to e.g. the age estimates of the observed source population.

Even so we note, given the limited analysis performed in this work, that the observed number of luminous SNe does not argue against a standard IMF in Arp 220. This conclusion is notably different from previous studies of the SNe/SNR population in Arp 220 which suggest a top-heavy IMF to explain the observed source population (see e.g. Parra et al. (2007)). We note that although Parra et al. (2007) used (a part of) the same raw data as analysed in this work, there are differences in calibration and imaging methods between the studies. In particular, there are significant differences for multiple sources between our work and previous studies using the same raw data (see Appendix C). A more thorough analysis of the data to constrain the IMF in Arp 220 should therefore include careful, detailed modeling of multiple of the compact sources to better constrain source ages. This is however beyond the scope of this work, and will be the subject of a future paper. In addition to the data presented here, this future work will include new global VLBI observations which are currently being scheduled. These data will help to further constrain the evolution of these objects and hence the rate of very luminous SNe in Arp 220.

4.3.4. The nature of the weaker objects

The majority of objects in Fig. 4 have luminosities below $5 \times 10^{27} \text{ erg s}^{-1} \text{ Hz}^{-1}$, and these sources are also (based on visual inspection of the lightcurves in appendix E) unlikely to have reached much higher luminosities during their evolution. The position of this population in Fig. 4 is consistent with these being smaller diameter versions of the ISM interacting SNRs in M82. Lacki & Beck (2013) argue that particles accelerated in the SNe in such environments as the nuclei of Arp 220 would have a maximum radiative lifetime of about a thousand years (see their Fig. 1). These calculations assume the electrons are embedded in an ISM magnetic field of 2 mG in Arp 220. In fact, fields in the SNR shells may be a factor of 10 larger (Batejat et al. 2011) and hence lifetimes shorter, but in this paper we assume a conservative figure of 1000 yrs. Given the SN-rate of 4 yr^{-1} , we would hence expect on the order of 4000 sources, which is a factor 50 more than we observe. Such an apparent discrepancy can however be explained if we are only detecting the most luminous SNRs from the most energetic supernova explosions in Arp 220 and the majority of SNRs are in fact below our detection limit.

Berezhko & Völk (2004) show that less energetic SNe expanding in lower densities reach lower peak luminosities at larger sizes (see their Fig. 4). This means such SNRs may only peak when larger than 0.5 pc and be missed by our surface brightness limited observations. In addition, the dependence of peak radio luminosity on explosion energy E_{sn} is very strong: in the Sedov phase the luminosity is expected to scale with $E_{\text{sn}}^{7/4}$, i.e. a factor of four less energy implies 10 times weaker peak luminosity. The simulations presented in Appendix D illustrate the effects of a range of explosion energies and the effect of limited surface brightness sensitivity on the detectability of the SNR population. In these simulations, only 55 of 1000 simulated sources are detected, clearly showing the impact of our limited surface brightness sensitivity. Note that although the simulations clearly illustrate the qualitative behaviour (i.e. limited sensitivity), the specific number of detected sources cannot easily be compared with the observed value. This is because of the significant uncertainties involved when e.g. setting the flux density scale of the simulations, as discussed in Appendix D.

We conclude that the fainter objects may very well be the tip of a distribution of supernova remnants, where the majority

have luminosities below our detection limit. Indeed, the brightest of these fainter objects sources, with diameter > 0.4 pc but $L_{6\text{cm}} < 3 \cdot 10^{28} \text{ erg s}^{-1} \text{ Hz}^{-1}$ (see Fig. 4), e.g. 0.2171+0.484, 0.2211+0.398, and 0.2360+0.431 are all consistent with being observed close to their 6 cm peak (see e.g. panel d in Fig. 2 and appendix E). Furthermore, these three sources are all long lived with stable lightcurves, indicating they did not evolve from the most luminous sources described above. Also, these sources show prominent 18 cm emission, indicating the blast wave has reached outside the ionised CSM.

4.4. The distribution of source sizes

We argue above that some small ($D < 0.4$ pc) and luminous $L_{6\text{cm}} > 5 \cdot 10^{28} \text{ erg s}^{-1} \text{ Hz}^{-1}$ objects are examples of the relatively rare radio luminous SNe, which interact strongly with a dense and ionised CSM. We also argue that the larger (and weaker) sources are SNRs, i.e. where the SN blast wave is interacting with the dense ISM. Two source populations are also consistent with the observed bimodal size distribution, see Fig. 7. However, while the two size-peaks may look well separated, there is likely significant confusion due to significant uncertainties when measuring sizes for weak sources (see appendix D). Hence, the small and weak sources observed in Fig. 4 are likely a mix of a few weak SNe which in a few years will reach $L_{6\text{cm}} > 5 \cdot 10^{28} \text{ erg s}^{-1} \text{ Hz}^{-1}$, a few less luminous SNe which will not reach $L_{6\text{cm}} > 5 \cdot 10^{28} \text{ erg s}^{-1} \text{ Hz}^{-1}$, and some large sources which due to low surface brightness (and perhaps also intrinsic shell asymmetry, e.g. as in SN1993J; Martí-Vidal et al. 2011a, their Fig. 9) appear shifted to small sizes.

4.5. A possible AGN candidate: 0.2227+0.482

The wealth of data now available on the compact sources in Arp 220 also enables us to search for evidence of AGN activity, which could be observed at GHz frequencies in the form of jet-like morphology, rapid variability, or a flat (or inverted) spectrum such as in e.g. Arp 299 (Pérez-Torres et al. 2010). One object, 0.2227+0.482 in the very centre of the western nucleus, has an inverted spectrum between 6 cm and 3.6 cm, as expected from an AGN, while the weak 18 cm emission could be explained by SSA or being very deeply buried in ionised gas causing free-free absorption. The radio lightcurves show a relatively rapid decline of an order of magnitude in luminosity in less than ten years, see Fig. 11. Extrapolating the 3.6 cm lightcurve assuming a common peak time for all frequencies then, given the evolution from 2006 and onwards, this source may have reached $L_{3.6\text{cm}} > 2 \cdot 10^{28} \text{ erg s}^{-1} \text{ Hz}^{-1}$, which is unusually bright compared to the other lightcurves in Appendix E.

The lightcurves alone are however not conclusive evidence for an AGN, as the observed lightcurves could also be explained as an energetic SN blast wave passing the boundary between a very dense CSM and very low density ISM, behind significant foreground free-free absorption. Indeed, the GC028 luminosities at 2 cm and 3.6 cm are consistent with an optically thin spectrum above 3.6 cm, where the low 6 cm emission and no 18 cm emission could be explained by significant free-free absorption. However, given that we only have one 2 cm epoch, and therefore are unable to e.g. search for systematic offsets in this particular epoch, this data point should be treated with care.

While significant absorption is certainly possible towards the centre of the nuclei, the ISM in the centre is thought to be very dense, and thus a rapid-decline scenario, which requires

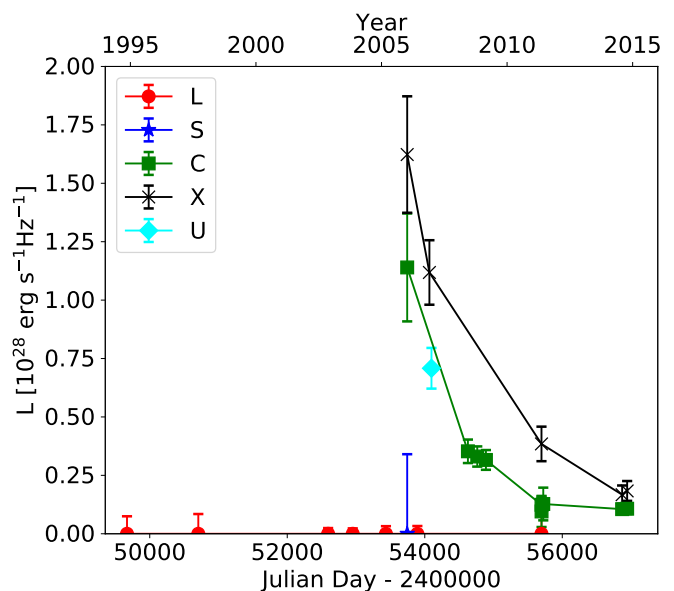


Fig. 11. The possible AGN candidate 0.2227+0.482 in the centre of the western nucleus, discussed in Sect. 4.5. Note that the vertical scale is different in this figure compared to other lightcurves in this paper to accommodate the unusually bright 3.6 cm emission detected in 2006.

the dense CSM to be surrounded by a very low-density ISM is unlikely. We also note that in addition to the lightcurves we measure a relatively small size (0.24 ± 0.29 pc) for this object, although the uncertainties are considerable given the relatively weak signal in the recent high-resolution observations. A strong stellar wind would have to encounter a very high-pressure ISM to be limited to such a small size. Furthermore, any AGN would likely be very massive and hence be situated in the centre of the local gravity field. Indeed, 0.2227+0.482 is located in the centre of the western nucleus and the position matches also very well the peak position of the 1.3 mm and 2.6 mm continuum reported by Downes & Eckart (2007), which they attribute to AGN activity, as well as the peak position of the 112.26 GHz ALMA dust continuum reported by Scoville et al. (2016).

4.6. Is the smooth GHz-emission of Arp 220 a collection of compact objects?

Barcos-Munoz et al. (2015) measure a total flux density of 222 mJy from Arp 220 at 4.7 GHz, seen at lower resolution as smooth synchrotron emission. The total flux density measured in the 91 continuum sources in Table 2 is 22.6 mJy, i.e. 10% of the total flux density. The fitted completeness level of the observed luminosity function in Sect. 3.5 and the detection limit shown in Fig. 4 strongly suggests that there are many more radiating sources in Arp 220 than we observe in this work. Could the sources below our VLBI surface brightness detection limit be the source of the smooth synchrotron emission detected by e.g. Barcos-Munoz et al. (2015)?

As a simple empirical estimate of the relative contribution of compact sources to the integrated flux density, we take the observed luminosity function and extrapolate this to luminosities below our detection threshold. If we assume all SNe give rise to an SNR, and an upper radiative lifetime of 1000 years, we expect, given the above SN-rate of about 4 yr^{-1} , about 4000 objects in Arp 220, of which we observe the brightest ~ 2 percent. Given a total number of 4000 SNRs, we can use Eq.5 to obtain a distri-

bution of $L_{\min} = 2.3^{+1.1}_{-0.9} \times 10^{25}$ erg s⁻¹ Hz⁻¹ (at 1.45 GHz) given a distribution of β . The distribution of A is determined from Eq. 5 assuming 79 sources brighter than our completeness limit as described above. If we integrate $n(L)L$ from L_{\min} to the observed $L_{\max} \approx 2 \times 10^{28}$ (at 1.45 GHz) we obtain the distribution of the total luminosity from compact sources as

$$L_{\text{tot}} = \int_{L_{\min}}^{L_{\max}} AL^{\beta+1} dL = \begin{cases} \frac{A}{\beta+2} (L_{\max}^{\beta+2} - L_{\min}^{\beta+2}), & \text{if } \beta \neq -2. \\ A \ln(L_{\max}/L_{\min}), & \text{if } \beta = -2. \end{cases} \quad (6)$$

As our fitted β is close to -2 we chose to calculate the total flux using both these expressions to check if they are similar. Starting with the first one ($\beta \neq -2$), and using 100,000 random draws of β (with mean -2.02 and $\sigma = 0.11$) we sample the distribution of L_{tot} to estimate uncertainties. Assuming $\alpha = -0.5$ we obtain a total 5 GHz flux density from 4000 compact sources of $L_{\text{tot}} 42^{+4.6}_{-4.3}$ mJy. As done above, the uncertainties correspond to $\pm 1\sigma$ for a Gaussian distribution, calculated using fitting to the sampled cumulative distribution function. If we instead assume that $\beta = -2$, we obtain the very similar value of $L_{\text{tot}} = 41.3$ mJy. We conclude that the integrated flux density from 4000 sources following the powerlaw distribution in luminosity defined by Eq. 4 can only account for about 20% of the total flux density observed from Arp 220 at GHz frequencies. So what is the source of the remaining radio emission?

The above argument assumes a maximum lifetime of CRs in the SN shocks of a thousand years. While the actual lifetime of accelerated CRs is likely shorter given the strong magnetic fields in the shocked regions (as noted in Sect. 4.3.4), the dense ISM in Arp 220 means that the SNR shocks will encounter significant particle densities also after leaving the CSM. Although each accelerated CR cools relatively quickly, the blast wave may possess significant kinetic energy for hundreds of years. During this time, particles in the ISM may be (re-)accelerated to emitting energies, long after the initial CRs accelerated in the ISM when entering the Sedov phase have faded. In addition, the massive progenitor stars likely form in dense star clusters of sizes of a few parsec (Wilson et al. 2006). In this case, SN shock waves with diameters larger than 1 pc (which may be too faint to be detected in Fig. 4) may collide with each other. The combined mechanical energy may be enough to compress the ISM to even higher densities and accelerate CRs to cause significant radio emission (Bykov 2014). In addition, given the high densities in Arp 220, also protons accelerated in the SN shocks may cause significant synchrotron radiation via collisions with ISM which produce secondary electrons and positrons, thereby more efficiently radiating the energy in the SN shocks (Lacki et al. 2010). This would imply that the fitted luminosity function has a significant tail of a large number of weak sources, compared to when extrapolated from the powerlaw in Fig. 9. This could potentially explain the origin of the smooth radio emission.

Another explanation could be an AGN contribution to the radio emission. However, a significant AGN contribution would likely manifest itself in a radio-bright compact core, and/or radio jets. While we do not find any clear support in terms of e.g. radio jets to support a recent significant AGN contribution to the radio emission (see Sect. 4.5), it is still possible that an AGN could play an important role in this galaxy, since its activity could be episodic and any jetlike structure dissolved into smoother structure by merger forces, and the emitting structure thereby hidden from VLBI observations due to lack of spatial scales sampled. Future observations with very high sensitivity, possibly combined with stacking of the current available data as well as tapering and statistical analyses of possible non-Gaussian contri-

butions to the image noise, may reach sufficient sensitivities to detect or exclude such a population of weak sources, and/or further constrain any AGN contribution.

5. Summary and outlook

In this paper we have presented data from 20 years of VLBI monitoring of Arp 220. We detect radio continuum emission from 97 compact sources, and find they follow a luminosity function $n(L) \propto L^{\beta}$ with $\beta = -2.02 \pm 0.11$, similar to normal galaxies. The spatial distribution of sources trace the star forming disks of the two nuclei seen at lower resolution.

We find evidence for a Luminosity-Diameter relation within Arp 220, where larger sources are less luminous. The exact form of the relation is however hard to quantify because of a range of selection effects. The observed distributions of source luminosities and sizes are consistent with two underlying populations. One group consists of very radio luminous SNe where the emitting blast wave is still inside the dense, ionised CSM. The other group consists of less luminous and larger sources which are thought to be SNRs interacting with the surrounding ISM.

In contrast to previous studies, we find that the observed number of very luminous SNe is consistent with expectations given a standard initial mass function and the total integrated star formation rate of the galaxy. This result should however be taken with care, as more detailed modeling of multiple sources is needed to better constrain the evolution, and in particular the ages, of the most luminous SNe.

We show that the apparent rapid structural variability reported by Batejat et al. (2012) can be explained in terms of convolution effects in regions with low surface brightness, rather than intrinsic source variability. However, we note the source 0.2227+0.482 as a possible AGN candidate, based on its observed lightcurves, measured size, and central position in the western nucleus.

When extrapolating the observed luminosity function below our detection threshold we find that the population make up at most 20% of the total radio emission from Arp 220 at GHz frequencies. However, secondary CR produced when protons accelerated in the SNRs interact with the dense ISM and/or re-acceleration of cooled CRs by overlapping SNR shocks may increase radio emission from the sources below our detection threshold, compared to the extrapolated value. This mechanism may provide enough emission to explain the remaining fraction of the total radio flux density, and could potentially be constrained by future high-sensitivity observations.

Continued high-sensitivity VLBI monitoring of Arp 220 will likely detect many more fainter sources and therefore probe the distribution of lower luminosities and larger sizes which may further constrain the evolution of SN/SNRs in extreme environments. Results from similar ongoing monitoring of other galaxies, such as the closer LIRG Arp 299 (Perez-Torres et al. in prep.) will be interesting for comparison to the results presented in this work.

Acknowledgements. EV, JC, SA, and IM-V. all acknowledge support from the Swedish research council. MAP-T and AA acknowledge support from the Spanish MINECO through grant AYA2015-63939-C2-1-P, partially supported by FEDER funds. The European VLBI Network is a joint facility of independent European, African, Asian, and North American radio astronomy institutes. Scientific results from data presented in this publication are derived from the project codes listed in Table 1. The National Radio Astronomy Observatory is a facility of the National Science Foundation operated under cooperative agreement by Associated Universities, Inc. This work made use of the Swinburne University of Technology software correlator, see Deller et al. (2011), developed as part of the Australian Major National Research Facilities Programme and operated

under licence. The Arecibo Observatory is operated by SRI International under a cooperative agreement with the National Science Foundation (AST-1100968), and in alliance with Ana G. Méndez-Universidad Metropolitana, and the Universities Space Research Association. This research made use of APLpy 1.0, an open-source plotting package for Python Robitaille & Bressert (2012).

References

- Alstott, J., Bullmore, E., & Plenz, D. 2014, *PLoS ONE*, 9, 1
- Arp, H. 1966, *ApJS*, 14, 1
- Barcos-Munoz, L., Leroy, A. K., Evans, A. S., et al. 2015, *APJ*, 799, 10
- Batejat, F., Conway, J. E., Hurley, R., et al. 2011, *ApJ*, 740, 95
- Batejat, F., Conway, J. E., Rushton, A., et al. 2012, *A&A*, 542, L24
- Berezhko, E. G. & Völk, H. J. 2004, *A&A*, 427, 525
- Bietenholz, M. F., Bartel, N., & Rupen, M. P. 2002, *ApJ*, 581, 1132
- Briggs, D. S. 1995, PhD thesis, The New Mexico Institute of Mining and Technology
- Bykov, A. M. 2014, *The Astronomy and Astrophysics Review*, 22, 1
- Chevalier, R. A. 1982a, *ApJ*, 258, 790
- Chevalier, R. A. 1982b, *ApJ*, 259, 302
- Chevalier, R. A., Fransson, C., & Nymark, T. K. 2006, *ApJ*, 641, 1029
- Chomiuk, L. & Wilcots, E. M. 2009, *ApJ*, 703, 370
- Clauset, A., Shalizi, C. R., & Newman, M. E. J. 2009, *SIAM Review*, 51, 661
- Cornwell, T. J. & Wilkinson, P. N. 1981, *MNRAS*, 196, 1067
- de Vaucouleurs, G., de Vaucouleurs, A., Corwin, Jr., H. G., et al. 1991, *Third Reference Catalogue of Bright Galaxies. Volume I: Explanations and references. Volume II: Data for galaxies between 0^h and 12^h. Volume III: Data for galaxies between 12^h and 24^h.*
- Deller, A. T., Brisken, W. F., Phillips, C. J., et al. 2011, *PASP*, 123, 275
- Downes, D. & Eckart, A. 2007, *A&A*, 468, L57
- Draine, B. T. & Woods, D. T. 1991, *ApJ*, 383, 621
- Dubner, G. & Giacani, E. 2015, *The Astronomy and Astrophysics Review*, 23, 1
- Eldridge, J. J., Fraser, M., Smartt, S. J., Maund, J. R., & Crockett, R. M. 2013, *MNRAS*, 436, 774
- Geen, S., Rosdahl, J., Blaizot, J., Devriendt, J., & Slyz, A. 2015, *MNRAS*, 448, 3248
- Greisen, E. W. 2003, *Information Handling in Astronomy - Historical Vistas*, 285, 109
- Haid, S., Walch, S., Naab, T., et al. 2016, *MNRAS*, 460, 2962
- Huang, Z. P., Thuan, T. X., Chevalier, R. A., Condon, J. J., & Yin, Q. F. 1994, *ApJ*, 424, 114
- Kettenis, M., van Langevelde, H. J., Reynolds, C., & Cotton, B. 2006, in *Astronomical Society of the Pacific Conference Series, Vol. 351, Astronomical Data Analysis Software and Systems XV*, ed. C. Gabriel, C. Arviset, D. Ponz, & S. Enrique, 497
- Lacki, B. C. & Beck, R. 2013, *Monthly Notices of the Royal Astronomical Society*, 430, 3171
- Lacki, B. C., Thompson, T. A., & Quataert, E. 2010, *APJ*, 717, 1
- Lonsdale, C. J., Diamond, P. J., Thrall, H., Smith, H. E., & Lonsdale, C. J. 2006, *ApJ*, 647, 185
- Lonsdale, C. J., Lonsdale, C. J., Diamond, P. J., & Smith, H. E. 1998, *ApJ*, 493, L13
- Marchili, N., Martí-Vidal, I., Brunthaler, A., et al. 2010, *A&A*, 509, A47
- Martí-Vidal, I. & Marcaide, J. M. 2008, *A&A*, 480, 289
- Martí-Vidal, I., Marcaide, J. M., Alberdi, A., et al. 2011a, *A&A*, 526, A142
- Martí-Vidal, I., Marcaide, J. M., Alberdi, A., et al. 2011b, *A&A*, 526, A143
- Martí-Vidal, I., Pérez-Torres, M. A., & Lobanov, A. P. 2012, *A&A*, 541, A135
- Martí-Vidal, I., Vlemmings, W. H. T., Muller, S., & Casey, S. 2014, *A&A*, 563, A136
- Mohan, N. & Rafferty, D. 2015, *PyBDSM: Python Blob Detection and Source Measurement, Astrophysics Source Code Library*
- Norris, R. P. 1988, *MNRAS*, 230, 345
- Parra, R., Conway, J. E., Diamond, P. J., et al. 2007, *ApJ*, 659, 314
- Pearson, T. J. 1999, in *Astronomical Society of the Pacific Conference Series, Vol. 180, Synthesis Imaging in Radio Astronomy II*, ed. G. B. Taylor, C. L. Carilli, & R. A. Perley, 335
- Pérez-Torres, M. A., Alberdi, A., Romero-Cañizales, C., & Bondi, M. 2010, *A&A*, 519, L5
- Petropoulou, M., Kamble, A., & Sironi, L. 2016, *MNRAS*, 460, 44
- Robitaille, T. & Bressert, E. 2012, *APLpy: Astronomical Plotting Library in Python, Astrophysics Source Code Library*
- Rovilos, E., Diamond, P. J., Lonsdale, C. J., Lonsdale, C. J., & Smith, H. E. 2003, *MNRAS*, 342, 373
- Rovilos, E., Diamond, P. J., Lonsdale, C. J., Smith, H. E., & Lonsdale, C. J. 2005, *MNRAS*, 359, 827
- Scoville, N., Murchikova, L., Walter, F., et al. 2016, *ArXiv e-prints*
- Scoville, N., Sheth, K., Walter, F., et al. 2015, *APJ*, 800, 70
- Smith, H. E., Lonsdale, C. J., & Lonsdale, C. J. 1998a, *ApJ*, 492, 137
- Smith, H. E., Lonsdale, C. J., Lonsdale, C. J., & Diamond, P. J. 1998b, *ApJ*, 493, L17
- Smith, N., Li, W., Filippenko, A. V., & Chornock, R. 2011, *MNRAS*, 412, 1522
- Varenius, E., Conway, J. E., Martí-Vidal, I., et al. 2016, *A&A*, 593, A86
- Vink, J. 2012, *A&A Rev.*, 20, 49
- Weiler, K. W., Panagia, N., Montes, M. J., & Sramek, R. A. 2002, *ARA&A*, 40, 387
- Wilson, C. D., Harris, W. E., Longden, R., & Scoville, N. Z. 2006, *ApJ*, 641, 763
- Wright, E. L. 2006, *PASP*, 118, 1711
- Yoast-Hull, T. M., Gallagher, J. S., & Zweibel, E. G. 2016, *Monthly Notices of the Royal Astronomical Society: Letters*, 457, L29

Table 2. List of the 97 sources analysed in this work. Δ R.A. and Δ Dec. are given with respect to the position R.A. $15^h34^m57.0000^s$ and Dec. $23^\circ30'11.000''$. Flux densities $F_{6\text{cm}}$ are measured by fitting a spherical shell to BB335B. Average diameters calculated according to Sect. 2.4 from the 3.6 cm and 6 cm measurements in experiments BB335A and BB335B.

Δ R.A. [s]	Δ Dec. ["]	Legacy name	Class	$F_{6\text{cm}}$ [μ Jy]	Average diameter [mas]
0.2066	0.458	W46	S-var	240 ± 35	2.04 ± 0.27
0.2082	0.548	W44	S-var	264 ± 36	1.63 ± 0.26
0.2084	0.534		Rise	198 ± 32	0.60 ± 0.29
0.2106	0.487		S-var	173 ± 30	2.11 ± 0.30
0.2108	0.512		Rise	458 ± 52	0.78 ± 0.20
0.2122	0.482	W42	Fall	511 ± 57	1.18 ± 0.19
0.2149	0.542		Fall	80 ± 26	1.02 ± 0.44
0.2154	0.450		S-var	90 ± 27	2.30 ± 0.71
0.2161	0.479	W40	S-var	223 ± 34	1.05 ± 0.27
0.2162	0.404	W41	S-var	118 ± 28	2.03 ± 0.45
0.2171	0.484	W39	S-var	389 ± 46	1.34 ± 0.23
0.2173	0.569		Fall	102 ± 27	2.37 ± 0.39
0.2194	0.507	W58	Rise	823 ± 86	0.64 ± 0.16
0.2195	0.492	W34	S-var	1210 ± 123	0.62 ± 0.13
0.2200	0.492	W33	Fall	193 ± 32	2.18 ± 0.29
0.2205	0.491	W56	S-var	1138 ± 116	0.70 ± 0.12
0.2211	0.398	W30	S-var	404 ± 47	1.81 ± 0.21
0.2212	0.444	W29	S-var	327 ± 41	2.48 ± 0.23
0.2212	0.540		Rise	93 ± 27	1.94 ± 0.70
0.2218	0.528		Rise	126 ± 28	0.45 ± 0.28
0.2222	0.500	W25	Fall	1066 ± 109	0.60 ± 0.13
0.2223	0.435	W26	S-var	238 ± 35	1.49 ± 0.26
0.2227	0.482	W55	Fall	139 ± 29	0.64 ± 0.29
0.2234	0.477		Rise	240 ± 35	0.41 ± 0.19
0.2239	0.470		S-var	71 ± 26	1.47 ± 0.29
0.2240	0.546	W18	S-var	726 ± 77	1.44 ± 0.16
0.2241	0.520	W17	S-var	373 ± 45	1.11 ± 0.21
0.2244	0.531	W16	S-var	323 ± 41	1.55 ± 0.24
0.2249	0.586		S-var	185 ± 31	2.18 ± 0.29
0.2253	0.483	W15	Fall	787 ± 82	0.95 ± 0.15
0.2262	0.512		Rise	351 ± 43	0.47 ± 0.22
0.2264	0.448		S-var	92 ± 27	1.34 ± 0.35
0.2269	0.574	W14	S-var	254 ± 36	2.35 ± 0.23
0.2276	0.546	W60	S-var	987 ± 102	0.52 ± 0.13
0.2277	0.528		S-var	67 ± 26	2.68 ± 0.35
0.2281	0.605		Fall	91 ± 27	3.15 ± 0.68
0.2286	0.583		S-var	132 ± 28	1.43 ± 0.52
0.2290	0.564		S-var	77 ± 26	3.08 ± 0.40
0.2295	0.524	W12	S-var	900 ± 93	0.70 ± 0.15
0.2299	0.502	W11	Rise	902 ± 93	0.90 ± 0.14
0.2306	0.502	W10	S-var	347 ± 43	1.93 ± 0.22
0.2310	0.496		S-var	< 25	2.69 ± 1.24
0.2311	0.498		S-var	121 ± 28	2.82 ± 0.30
0.2317	0.402		Rise	64 ± 26	2.27 ± 0.83
0.2347	0.495		Rise	109 ± 27	2.65 ± 0.42
0.2360	0.431	W8	S-var	399 ± 47	2.44 ± 0.21
0.2362	0.546	W7	Fall	333 ± 42	2.92 ± 0.22
0.2363	0.369		Fall	116 ± 28	0.66 ± 0.37
0.2364	0.639		S-var	39 ± 25	2.00 ± 1.07
0.2394	0.540	W2	S-var	203 ± 32	1.82 ± 0.30
0.2395	0.637		S-var	61 ± 26	4.83 ± 1.21
0.2409	0.540		Rise	104 ± 27	0.65 ± 0.41
0.2758	0.276		Rise	96 ± 26	4.64 ± 0.42
0.2789	0.293		S-var	105 ± 26	2.95 ± 0.68
0.2801	0.353		S-var	58 ± 25	4.25 ± 1.21
0.2814	0.316		S-var	66 ± 25	2.10 ± 0.48
0.2821	0.183	E20	S-var	195 ± 31	3.05 ± 0.38
0.2835	0.308		S-var	130 ± 27	3.78 ± 0.62
0.2840	0.151		S-var	< 24	2.80 ± 1.08

Table 2. continued.

$\Delta R.A.$ [s]	$\Delta Dec.$ ["]	Legacy name	Class	F_{6cm} [μJy]	Average diameter [mas]
0.2842	0.226	E18	S-var	119 ± 27	2.20 ± 0.58
0.2848	0.294		Fall	87 ± 25	1.39 ± 0.82
0.2848	0.471	E16	S-var	89 ± 26	2.32 ± 0.44
0.2850	0.193	E17	Fall	106 ± 26	2.93 ± 0.75
0.2858	0.013		S-var	< 24	N/A
0.2868	0.297	E14	S-var	578 ± 62	0.89 ± 0.16
0.2875	0.352		Fall	132 ± 27	2.64 ± 0.24
0.2878	0.308	E13	S-var	201 ± 31	3.02 ± 0.36
0.2881	0.369		Rise	159 ± 29	0.73 ± 0.33
0.2883	0.338		S-var	118 ± 27	1.97 ± 0.29
0.2887	0.201		S-var	170 ± 29	1.07 ± 0.31
0.2890	0.337		S-var	112 ± 26	0.96 ± 0.35
0.2891	0.253		S-var	80 ± 25	2.29 ± 0.44
0.2897	0.278		S-var	100 ± 26	2.27 ± 0.59
0.2897	0.335		S-var	161 ± 29	0.91 ± 0.26
0.2910	0.325	E11	S-var	184 ± 30	1.80 ± 0.27
0.2914	0.333		Fall	221 ± 32	1.03 ± 0.25
0.2915	0.335	E10	Fall	907 ± 93	0.59 ± 0.12
0.2915	0.476		Fall	40 ± 24	0.62 ± 1.46
0.2919	0.340		S-var	93 ± 26	1.58 ± 0.40
0.2928	0.373	E24	S-var	313 ± 39	1.26 ± 0.21
0.2931	0.330	E8	S-var	76 ± 25	1.10 ± 0.59
0.2938	0.344		Fall	24 ± 24	2.03 ± 0.43
0.2940	0.481		S-var	130 ± 27	3.44 ± 0.61
0.2943	0.279	E7	S-var	135 ± 27	2.44 ± 0.45
0.2947	0.263	E6	Fall	79 ± 25	2.02 ± 0.66
0.2951	0.384		Rise	216 ± 32	0.67 ± 0.30
0.2954	0.393		S-var	121 ± 27	2.98 ± 0.59
0.2959	0.263		S-var	96 ± 26	2.96 ± 0.50
0.2971	0.378		Fall	62 ± 25	3.16 ± 0.29
0.2979	0.419		S-var	138 ± 28	2.04 ± 0.27
0.2995	0.502		S-var	59 ± 25	0.65 ± 0.55
0.3011	0.341		Rise	323 ± 40	0.51 ± 0.21
0.3073	0.332	E3	S-var	77 ± 25	2.18 ± 0.59
0.3073	0.456		S-var	48 ± 24	1.88 ± 1.00
0.3090	0.618		N/A	< 24	N/A
0.3103	0.575		N/A	< 24	N/A
0.3125	0.494		S-var	< 24	2.85 ± 0.81

Appendix A: Calibration and imaging

Appendix A.1: Phase calibration and positional uncertainty

For most epochs phase calibration started by removing bulk residual delays and rates, using one of the three bright sources J1516+1932, J1613+3412 or OQ208 by running the AIPS task FRING. This should also remove relative phase differences between the spectral windows (AIPS IFs). However, multiple epochs showed time variable phase differences between the IFs. This was corrected for by running FRING also on the phase-reference source J1532+2344 for epochs where this source was included in the observations.

Experiments *BP129*, *GC028*, *GC031*, *BB297* and *BB335* were all phase-referenced to the nearby (0.55°) compact calibrator J1532+2344, assumed to be located at R.A. $15^h32^m46^s.3452$, Dec. $23^\circ44'05''.268$, and Arp 220 was correlated at position R.A. $15^h34^m57^s.250$, Dec. $23^\circ30'11''.33$, i.e. between the two nuclei. After transferring the phase-reference corrections, an initial image was made of Arp 220. In many cases, the resulting image showed beam like artefacts around bright sources consistent with residual phase errors. To remove the residual phase-errors, phase self-calibration (see e.g. Cornwell & Wilkinson 1981) was used with the initial phase-referenced image as calibration model.

The self-calibration step removed obvious phase-errors, and generally improved the images. However, because Arp 220 is weak at mas-scales (5-35 mJy in these data), a low baseline SNR threshold of 2 was required. Such a low threshold may introduce spurious sources or in other ways impact the data in a negative way (Martí-Vidal & Marcaide 2008). To assure the validity of the self-calibrated results, we checked

1. The general image quality: Did the self-calibration cycle remove obvious phase-errors, such as convolution like artefacts on all sources?
2. The RMS noise in central regions with many sources: Did it decrease after self-calibration?
3. The source flux densities: Did the source flux densities increase as expected after self-calibration?
4. The phase-solutions: Although noisy, were the solutions tracing slowly varying atmospheric errors and/or clear antenna offsets?
5. The consistency with all available data: Were the flux densities and sizes, measured for a particular epoch, consistent with the information from all other epochs?

In summary, we found clear signs of improvements in image quality for most epochs, and no clear sign of corruption due to self-calibration. We note that we only performed one cycle of self-calibration, which leaves little room for spurious sources to grow bright, as can sometimes happen after many cycles of poorly constrained self-calibration. We note that only phase-corrections, i.e. no amplitude corrections, were derived using self-calibration of Arp 220.

In contrast to the phase-referencing above, four 18 cm experiments, *GL021*, *GL026*, *GD017*, and *GD021*, were phase-referenced to compact OH-maser emission within Arp 220 itself. Phase corrections were derived from self-calibration using the strongest maser channel. Initially, a point source model was used, but in all cases the elongated structure of W1 (see Lonsdale et al. (1998), their Fig. 1a) was recovered after a single iteration. One or two additional self-calibration iterations were carried out to ensure the structure of the maser was correctly taken into account. The corrections derived for this single channel were then

applied to all channels of all spectral windows. No further self-calibration of Arp 220 was performed for these epochs. Note that no high-resolution spectral data were used (although in some cases available in the archive). Instead, we used a single broad frequency channel in the continuum data, containing the maser emission, to obtain corrections for residual phase errors.

The three 18 cm experiments *GL021*, *GL026*, and *GD017* assumed a correlation position of R.A. $15^h34^m57^s.2247$, Dec. $23^\circ30'11''.564$ for Arp 220, while *GD021* used the same as *BP129*. By phase self-calibration of the brightest maser channel (in the continuum data), the position of all compact sources were anchored to the peak of the compact maser. In this work, we assume a peak position of the maser W1 of R.A. $15^h34^m57^s.22435$, Dec. $23^\circ30'11''.6644$. This position was obtained from imaging the maser emission in the phase-referenced 18 cm data taken in experiment *BB297A*. Since *BB297A* was phased-referenced to J1532+2344 (and did not use the maser for phase calibration), we thereby align the maser calibrated epochs to the common reference position of J1532+2344 used for the other epochs. We assume that the maser position does not vary between the observations. Cross-correlation of the resulting continuum images among the different epochs supports this assumption.

Given that many sources are close to our surface brightness detection limit, and the fact that many are resolved which may impact the peak position, we assume a conservative uncertainty of 1 mas for all source positions within Arp 220. Notes on position offsets for particular sources can be found in Appendix C.2.

Appendix A.2: Amplitude calibration

The amplitude calibration of all epochs was anchored to the measurements of system temperatures and gains of VLBA antennas. The procedure applied to ensure the best possible amplitude calibration was as follows:

1. Apply a priori amplitude calibration to all antennas, using measured system temperatures and antenna gain curves.
2. Determine a set of good, self-consistent, antennas (usually the VLBA), excluding antennas with obvious amplitude offsets seen in amp vs. UV-distance plots.
3. Perform amplitude self-calibration of the good antennas to correct minor errors, using imaging of a bright observed source, i.e. J1516+1932, J1613+3412 or OQ208, depending on data set.
4. Amplitude self-calibration of previously excluded antennas, fixing the good antennas, using the same bright source. This forces even very sensitive antennas to the correct absolute flux scale. We note that if sensitive antennas with a major error are included from the start, the whole flux scale may be shifted due to their large weight.
5. Either, for phase-referenced epochs: derive amplitude corrections for the target by imaging and (self-)calibrating the phase-reference source, or,
6. For some maser-calibrated epochs: derive amplitude corrections for the target by imaging and (self-)calibrating the maser emission.
7. Apply cumulative antenna based corrections to the Arp 220 observations.

We adopt an absolute flux calibration uncertainty of 10% for all data.

We note that the noise we obtained in some re-reduced observations is larger than in some previous publications (e.g. Lonsdale et al. 2006). This may be explained by several factors. First,

multiple non-VLBA antennas had to be excluded from our processing, since no system temperatures or gain measurements could be found (these seem to have been lost as they are not available via e.g. the NRAO or JIVE online archives). Second, because of the large amount of data processed in this work and our efforts to use a similar calibration and imaging strategy for all data, we may have missed opportunities to improve specific epochs by e.g. elaborate weighting of very sensitive antennas, or extra careful editing of bad data. Still, we found the resulting images to be of sufficient quality.

For the 6 cm data sets GC031B and GC031C, a careful analysis of the final images, made after using the calibration strategy outlined above, revealed both these epochs to be systematically too bright for all sources, although their relative flux densities were reasonable. These offsets were also found when comparing the amplitudes of the uncalibrated visibilities on multiple VLBA baselines to the corresponding baselines in BP126 and BB297A. We also found consistent offsets in the recovered flux densities of the bright calibrator J1516+1932 in these epochs. We believe that these epochs were affected by an error, scaling the visibilities to higher values before storing them in the archive. Further investigations of this error is however beyond the scope of this work. For the purpose of this work, we derive a scaling factor for each of the two epochs, based on a requirement of continuity for the light-curves of the brightest sources, as well as the observed differences in the raw uncalibrated visibilities. The correction factor derived for both epochs was 0.70, and it was applied to the images before any analysis of these epochs.

Appendix A.3: Bandpass calibration

For all epochs, bandpass corrections were derived using a bright observed source, i.e. J1516+1932, J1613+3412 or OQ208, depending on data set, assuming these sources to have a flat spectrum across the observing bandwidth.

Appendix A.4: Imaging

All epochs were imaged using the task IMAGR in AIPS, using two fields to simultaneously clean the two nuclei. All epochs were imaged in a two-step auto-boxing procedure, as implemented in IMAGR. First, boxes were automatically placed by IMAGR on the brightest sources, defined as having peak signal-to-noise > 10 and source island level > 5 . This minimised the risk of cleaning strong side lobes caused by the synthesised beam. Then, the boxes were removed and a few hundred clean iterations ran without any box-restrictions to find weaker sources. The imaging was stopped when the peak of the clean components reached the random noise. The final images were exported to FITS for further analysis outside AIPS. The pixel dimensions used were 8192 in R.A. and Dec. for all images. For the 2 cm data, a cell size of 0.05 mas was used. All other epochs used a cell size of 0.1 mas. Robust weighting (Briggs 1995) of 0.5 was used for all images.

Appendix B: Model fitting

In principle, it is best to fit models directly to the calibrated visibilities, instead of the cleaned images, to avoid any effects introduced by the deconvolution (e.g. Martí-Vidal et al. 2014). However, the amount of data processed in this work make visibility fitting impractical. We therefore decided to fit models to the cleaned images. Using the images is faster mainly because we

can work on a small subimage encompassing each source. This makes the fitting very quick, a few seconds per source. However, since the sources are smaller than or comparable to the synthesised beam, sub-pixel accuracy is required to avoid the fitting algorithm converging to local minima. This can be achieved by fitting the data to analytical models in Fourier space, although using a Fourier transform of the cleaned image instead of the measured visibilities themselves. Below we describe in detail how the fitting was done for each source.

First a small subimage, hereafter called a stamp, was extracted from the cleaned image, centred on the source catalogue position in Table 2. The stamp was selected as 128×128 pixels at bands C and X, and 256×256 pixels at bands L, S and U. To avoid fitting in epochs with very low signal, or negative noise spikes, a simple check of signal strength was performed. A region of 2×2 mas in the centre of the stamp was checked to have a peak value of at least three times the cleaned image off-source RMS noise (given in Table 1). If not, fitting was not performed for this source in this epoch. If the stamp was strong enough, it was transformed to the Fourier domain using the Python library `numpy.fft.fft2`.

A source model was then defined in Fourier Space in the form of an optically thin spherical shell. The basis was the Fourier transform of an optically thin sphere with flux density 1 as listed in Pearson (1999), their eq. 16-28. A shell was obtained by subtracting an inner sphere with diameter d_i from an outer sphere with diameter d_o where $d_i = 0.7d_o$ and both spheres were scaled to have flux densities equal to their respective volumes. The resulting shell was then scaled to a desired flux density.

The shell was multiplied in the Fourier domain by the Fourier transform of the CLEAN beam, defined as a two dimensional Gaussian function, i.e. equivalent to convolving the model with the CLEAN beam in the image domain. A residual fitting function was defined as the difference between the convolved shell and the source stamp. The function was minimised using the Python library `scipy.optimize.least_squares` which enables bounded least-squares fitting. The minimisation was allowed to simultaneously vary the flux density, size, and position of the shell. The flux density was required to be $\geq 3\sigma$, the size ≤ 5 mas, and the position in R.A. and Dec. was restricted to be within ± 1 mas of the stacked catalogue position listed in Table 2. The initial guess was the same for all fits: flux density 0.5 mJy, size 0.1 mas (1 pixel), and position as in Table 2.

Most sources were very well centred, but a few clearly resolved shells had minor offsets since the PyBDSM algorithm had found the peak at one side of the shell. An example of this can be seen in Fig. B.1. When the fit converged, the best-fit model was transformed to the image plane and subtracted from the working-copy of the cleaned image to simplify fitting of other nearby sources. Finally the best-fit parameters were saved to disk.

Appendix B.1: Comparison with other fitting methods

Tests done on multiple test sources to compare visibility fitting with our image based method show a good agreement. Our values are also in good agreement with the statistical method used in Batejat et al. (2011), as seen in Fig. C.1 where the minor differences could be due to differences in calibration and imaging strategies. Hence we are confident that our method obtains robust results.

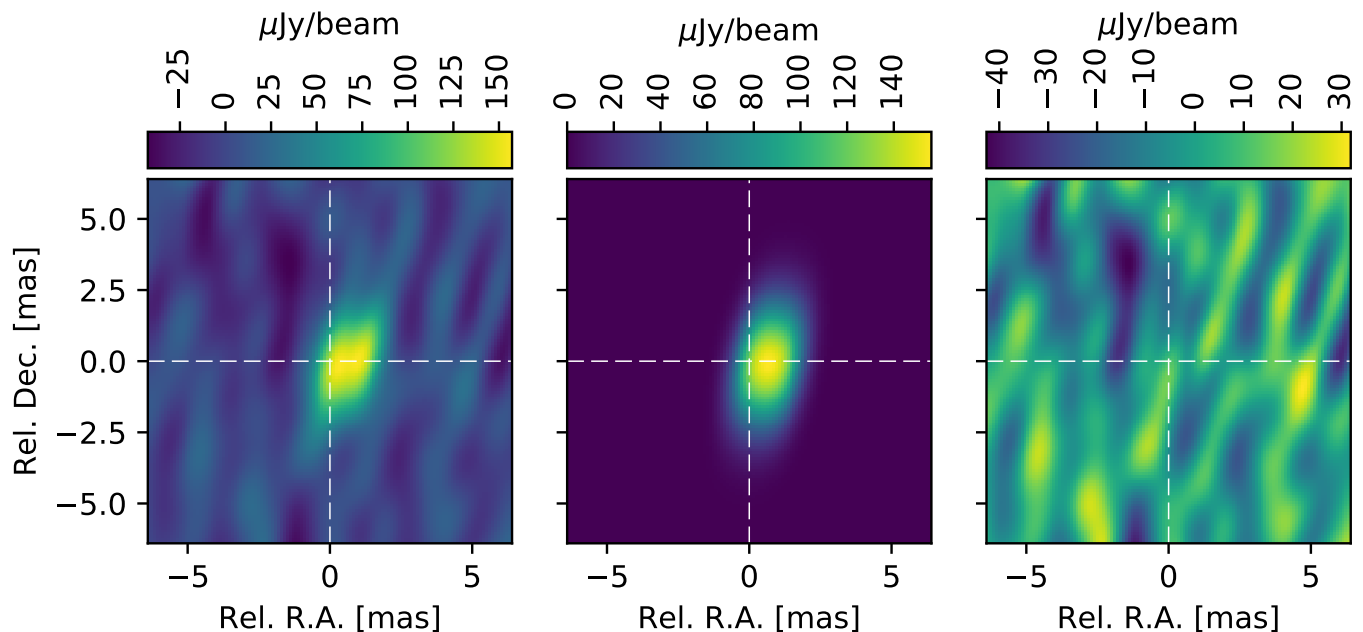


Fig. B.1. Example fitting of a clearly resolved source 0.2212+0.444 in the 6 cm image of BB335B. The left panel shows the CLEANED image (the observation), the mid panel the best fit model convolved with the CLEAN beam, and the right panel the residual i.e. image–model. The white cross marks the centre of each panel, i.e. the position guess obtained from PyBDSM. This particular fit was chosen because it shows that the position found by PyBDSM may be off when PyBDSM’s Gaussian fitting finds the peak of one of the two beam-features of a weak resolved shell. However, since the position is allowed to vary, this taken into account in the fitting, as seen here where the fitted position is a little to the right of the white cross.

Appendix B.2: A self-consistent check of the catalogue positions

The source positions in Table 2 were obtained by PyBDSM as described in Sect. B. However, one may ask, do the stacked images really provide a good reference for the catalogue, or for initial guesses for the fitting routine, given that some sources may appear variable (as discussed in Sect. 3.3)? To check this we compiled two figures of the difference between the catalogue R.A. and Dec. and the fitted R.A. and Dec for all modelfits done in this work, see Fig. B.2.

The majority of fitting results are well within our target accuracy of ± 1 mas. Note that 18 cm fits are not included in this figure; the spread in R.A. is very similar for 18 cm, but the fitting in Dec. is much less well constrained because of the relatively large major axis of the synthesised beam which in most epochs extends towards north-south. However, the freedom in the fitting to find the best fit within ± 1.5 mas enables the fitting to find good results also at 18 cm.

Appendix C: A comparison of source properties with published literature

In this section we present comparisons done between our fitted values for the compact sources and values available in the literature.

Appendix C.1: Source catalogues and completeness

To compare our results with previously published values we tried to match our detected sources with the positions published by Lonsdale et al. (1998, 2006); Parra et al. (2007); Batejat et al. (2011). The matching was done by comparing coordinates both

automatically and manually to account for typos and blending effects, as mentioned in Sect. C.2, and in general the difference between our positions and the literature positions were much less than the beam size. When we found matches we have included the legacy name (e.g. W55, E8) in Table 2. Even though we accounted for different reference positions, as noted in Sect. C.2, we found no counterpart in our images for the following sources: W3, W9, W19, W24, W27, W28, E4, E12, E19. These may be false positives in previous studies, but it is also possible that they were weak when detected and has been declining since. Although we re-analyse the data used by e.g. Lonsdale et al. (2006), our images are not as deep as the ones previously published. Hence we may miss sources both in these old epochs due to the lower sensitivity, and in our recent 5 GHz epochs due to declining lightcurves and steep source spectra. Further investigation of these sources are beyond the scope of this work.

Appendix C.2: Positions of particular sources

As noted by Parra et al. (2007), the maser reference position assumed by Lonsdale et al. (2006) and previous studies was off by about $0.1''$ in declination, with a declination of $11.564''$ being assumed instead of $11.664''$, as noted above. However, from cross-referencing of the relative source positions listed in Lonsdale et al. (2006), their Table 1, with the positions obtained in this work, we find the reference position used for the relative coordinates listed by Lonsdale et al. (2006) at R.A. $15^h 34^m 57^s.26255$, Dec. $23^\circ 30' 11''.352$, i.e. different from the maser peak position used for phase referencing. This difference has been taken into account when comparing positions and flux densities for these sources.

We note that the R.A. position listed by Lonsdale et al. (2006) for W11 corresponds to $57^s.2300$, which is consistent

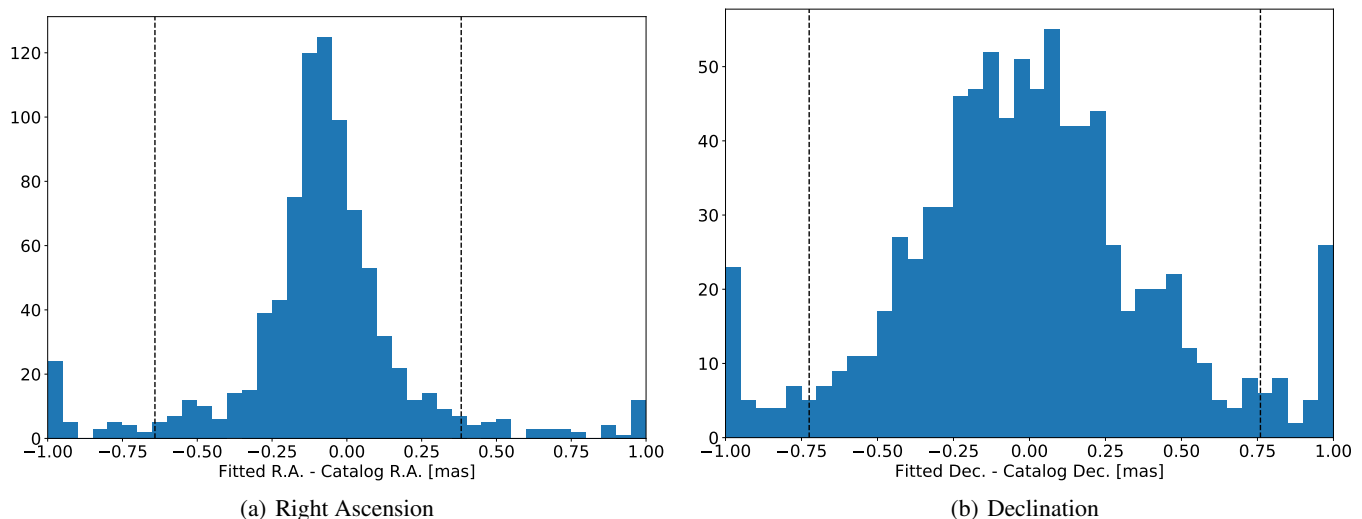


Fig. B.2. Comparison of fitted positions with catalogue positions given in Table 2. The dashed lines mark the 5% and 95% percentiles. The majority of fitting results are well within our target accuracy of ± 1 mas. The larger dispersion in Dec. compared to R.A. is explained by the synthesised beam being elongated approximately north-south in most epochs. Note that 18 cm fits are not included in this figure; the spread in R.A. is very similar for 18 cm, but the fitting in Dec. is much less well constrained because of the relatively large major axis of the synthesised beam.

with the position we find as well as the position listed by Batejat et al. (2011). However, in Parra et al. (2007) this source is listed with R.A. $57^s.2230$ which seems to be a typographical error. Furthermore, the position listed for E11 by Lonsdale et al. (2006) corresponds to our source $0.2910+0.325$, which is about 10 mas from the source $0.2195+0.335$ (E10). However, we also find a source $0.2913+0.333$ situated between these two sources, only about 3 mas from $0.2195+0.335$. From Table 1, it is clear that observations at wavelengths longer than 6 cm do not have sufficient resolution to distinguish the two sources $0.2195+0.335$ and $0.2913+0.333$, and hence the flux densities measured at 1.4 GHz for these two sources, also in this work, should be interpreted with caution. We note that Batejat et al. (2011) associated $0.2913+0.333$ with the previously listed source E11 instead of associating $0.2910+0.325$ with E11 as we have done. Although $0.2195+0.335$ and $0.2913+0.333$ may be confused at 1.4 GHz, the resolution is good enough to separate $0.2913+0.333$ and $0.2910+0.325$. We therefore believe that Batejat et al. (2011) misidentified $0.2913+0.333$ as E11, likely because $0.2910+0.325$ is weaker at 6 cm than $0.2913+0.333$, and hence their spectrum for E11 should be interpreted with caution.

To avoid typographical errors in this paper we have generated all figures and tables in the paper directly from the source catalogues generated by the source-finding algorithm as described in Sect. 2.1, without any manual editing.

Appendix C.3: Flux densities and sizes

As stated previously, some data included in this work have been published before. In Fig. C.1, we compare the flux densities and sizes measured in this work with previously published values.

Flux densities for the epochs GD017 and BP129 were reported by Parra et al. (2007), where the 18 cm values observed in 2003 (GD017A) were taken from Lonsdale et al. (2006). In Fig. C.1 (panel a), we compare the flux densities recovered in this work to those previously published by Parra et al. (2007). We find that we in general find larger values, although the scaling factor varies between publications and data sets. Notably, we measure approximately two times higher flux densities than

previously reported for all BP129. Since we find that our fitting method produces good results compared to e.g. manual inspection of the images (which was the method used to extract the flux densities by Parra et al. (2007) for BP129) we believe this flux discrepancy is due to differences in calibration and imaging strategy. However, a factor of two is much larger than expected given the uncertainties of the measurements. We use the same calibration strategy for BP129 as for other epochs. We have checked our calibration scripts for BP129 carefully without finding any reason for too high flux densities. We therefore suspect that values reported for BP129 by Parra et al. (2007) suffer from a systematic error in the calibration or imaging strategy, giving too low flux densities. We note that the image noise levels reported by Parra et al. (2007) are very similar to the noise we obtain. This argues against a simple difference in how the flux scale was set. Instead, such a flux density reduction suggests incoherent addition of visibilities, i.e. with strong phase errors present in one or more antennas during a significant period of time. We note that self-calibration could increase the flux density of sources in many epochs, which should reduce the RMS noise in the image. However, we see, for example for the GD017-epochs, an increase in both RMS noise level and source flux density compared to previous publication. Such an increase could instead be attributed to differences in amplitude calibration strategy, where our careful alignment of potentially bad antennas using bright sources should provide a more accurate amplitude scale. Further investigation of the details of the calibration performed by Lonsdale et al. (2006) and Parra et al. (2007) is beyond the scope of this paper.

Flux densities for epochs GC028 and GC031A are reported in Batejat et al. (2011), together with a revised version of the flux densities for the 6 cm data of BP129 (the 13 cm and 3.6 cm values for BP129 are taken directly from Parra et al. 2007). In Fig. C.1 (panel b), we compare the flux densities recovered in this work to those previously published by Batejat et al. (2011). We find the flux densities reported for GC031A to be in excellent agreement with our measurements. However, we measure flux densities to be 1.5 times higher than reported for GC028 and BP129-C by Parra et al. (2007). Again, using the same ar-

gument as in the previous paragraph, we assume that our new values are correct. We note that Batejat et al. (2011) claim an image noise of $41 \mu\text{Jybeam}^{-1}$ for BP129-6 cm, which is a factor of two lower than what we obtain. We note that while Batejat et al. (2011) left multiple sources unclassified due to inconsistent lightcurves, we find, given our higher flux density values for some epochs, the lightcurves for these sources consistent with SNe/SNR evolution, as noted in Sect. C.4.

Source sizes were reported by Batejat et al. (2011) using data at 2 cm and 3.6 cm. In Fig. C.1 (panel c), we compare the sizes given in Batejat et al. (2011) with our measurements from the same data. We only include the 12 sources where diameters are given in Batejat et al. (2011), their Table 3, i.e. not the sources with only upper limits. The sources fitted in both epochs by Batejat et al. (2011), i.e. bold face in their Table 3, are shown as stars in our Fig. C.1, while the remaining sources are shown as circles. As new diameters, we take the average of the fitted values for the 2 cm and 3.6 cm images, as done by Batejat et al. (2011). We find the measurements to be in good agreement, except for the smallest sources which are the hardest ones to measure, given the limits in image resolution.

Appendix C.4: Source classifications

The number of sources detected in this work is too large for a detailed discussion on each object. However, in this section we discuss the classification of a few particular sources where previous studies have suggested AGN activity.

The source 0.2171+0.484 (W39) was left unclassified by Batejat et al. (2011) because it showed declining luminosity at long wavelengths and increasing luminosity at short wavelengths. After re-analysing the data, we find 0.2171+0.484 to have stable or declining lightcurves at all frequencies with a powerlaw spectrum, consistent with an SNR scenario where the blast wave is interacting with the ISM.

The source 0.2915+0.335 was also left unclassified by Batejat et al. (2011) as it showed declining luminosity at long wavelengths and increasing luminosity at short wavelengths. We instead find the lightcurves for 0.2915+0.335 to decline at both 6 cm and 3.6 cm, with approximately the same flux densities in both bands. Little or no emission is detected at 18 cm. The faint 18 cm emission and fact that the 6 cm emission is not significantly brighter than the 3.6 cm emission may indicate significant internal and/or external free-free absorption. Although 0.2915+0.335 is today declining at 6 cm and 3.6 cm, it emitted close to $1.5 \times 10^{28} \text{ erg s}^{-1} \text{ Hz}^{-1}$ at these wavelengths in 2006. It is hence similar to our AGN candidate 0.2227+0.482, but the 6 cm and 3.6 cm lightcurves show a significantly slower decline for 0.2915+0.335. Given the relatively small measured size of 0.2 pc, the weak 18 cm emission, this source may be a relatively young SN where the shock is interacting with a dense ionised CSM.

We note that, as discussed in Sect. 3.3, the three sources reported as variable by Batejat et al. (2012) are likely large SNRs. Similarly, 0.2200+0.492 (W33), listed as consistent with an AGN morphology by Batejat et al. (2011), is likely an SNR. Finally, the three sources 0.2306+0.502 (W10), 0.2241+0.520 (W17), and 0.2122+0.482 (W42), noted as flat-spectrum AGN candidates by Parra et al. (2007), are likely SNRs.

Appendix C.4.1: OH-maser sources

We note that in addition to the continuum sources, we also detect, in our 18 cm observations, three sources in OH-maser emission, without any continuum counterpart, at positions 0.2243+0.665, 0.2957+0.341, 0.2912+0.219. We identify these as the maser objects W1, E1, and E2 discussed by Lonsdale et al. (1998). These sources are however not included in Table 2 as a discussion of the OH-maser emission in Arp 220 is beyond the scope of this work. We refer the interested reader to e.g. Lonsdale et al. (1998); Rovilos et al. (2003).

We note, however, that at the position of the OH-maser listed as W2 by Lonsdale et al. (1998), we find a clear (although relatively weak) continuum counterpart 0.2394+0.540 at multiple epochs and frequencies with stable or declining lightcurves. Based on the available data we conclude that this source is likely an SNR.

Appendix D: Simulation of the SNR evolution and uncertainties in size fitting

To illustrate the effects of a range of explosion energies combined with limited surface brightness sensitivity, we performed a Monte Carlo simulation of an SNR population. Although a number of studies have investigated how individual SN blast waves interact with CSM and eventually the surrounding ISM (e.g. Geen et al. (2015); Haid et al. (2016)) as well as radio emission from generic SNRs in normal galaxies (Berezhko & Völk 2004), there are to the best of our knowledge no detailed simulations of radio emission for the high ISM densities of $\sim 10^5 \text{ cm}^{-3}$ (Scoville et al. 2015) as expected in Arp 220. Given this we have to make assumptions that similar principles governing the radio emission and dynamics of SNRs in the lower density ISM of normal galaxies apply also to the objects in Arp 220.

To sample the SNR evolution we created 1000 sources with ages uniformly distributed in the range 30-1000 years, where the latter limit is the estimated lifetime of the accelerated CRs. The SNR diameters were then obtained as a function of SNR age from the blast wave dynamics model presented by Draine & Woods (1991) for a medium of uniform density, i.e. ignoring the effects of any initial CSM phase, which will not strongly affect the results for radius versus time for SNRs at their Sedov radius and beyond. In detail, the SNR diameter was calculated from numerical integration of the inverse expression $t(R)$ given by Draine & Woods (1991) (their Sect. 4), using their equations 4.1, 4.2, 4.4, 4.5, 4.10, 4.15 and 4.16, which gives the shock velocity and age as a function of radius, where we assumed $n_{H_2} \sim 5 \cdot 10^4 \text{ cm}^{-3}$, an ejecta mass of $10 M_{\odot}$, and an explosion energy $E_{51} = 3 \cdot 10^{51} \text{ ergs}$ (for the most luminous objects).

Given a population of diameters, we assumed the relationship $L \propto D^{9/4}$ for SNRs (Berezhko & Völk 2004, their Eq. 35) normalised so that a source with diameter 0.2 pc had a 6 cm luminosity of $0.6 \times 10^{28} \text{ erg s}^{-1} \text{ Hz}^{-1}$, i.e. similar to the observed LD-relation in Fig. 4.

Berezhko & Völk (2004) predict that the luminosity of an SNR is expected to depend strongly on the explosion energy as $L \propto E_{\text{sn}}^{7/4}$ (their Eq. 35). It is not clear whether exactly the same dependence would apply for higher density environments, but to simulate a range of explosion energies each source luminosity was scaled with a random number drawn from a uniform distribution in the range 0.1-1.0 (corresponding to a range in energy of 3-4). Each pair of L-D values were now used to produce a simulated image of a spherical shell (with fractional

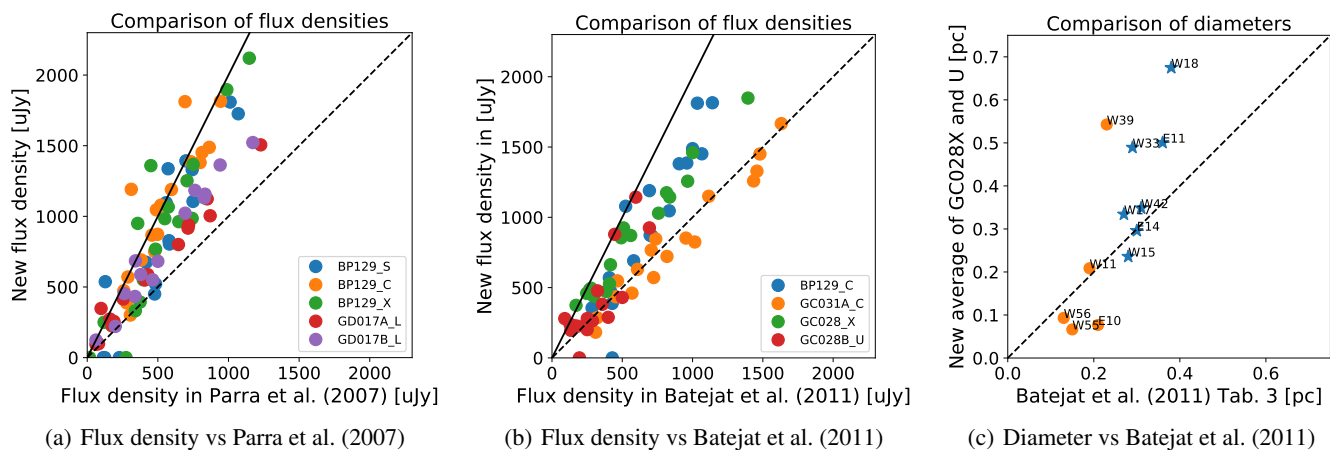


Fig. C.1. Comparison of flux densities and sizes measured in this work with previously published values using the same data. The dashed lines indicate a one-to-one correspondence, and the solid lines indicate the new values to be a factor of 2 higher than the ones previously published. In Fig. 1c, stars mark sources resolved at both bands by Batejat et al. (2011) (bold face in their Table 3) while circles mark the remaining sources. See Sect. C for a discussion of discrepancies.

width 30%) convolved with the CLEAN beam from the 6 cm experiment BB335B.

In addition to variation of intrinsic parameters, the image noise can affect the measurements, in particular for weak, large sources close to the surface brightness sensitivity (as discussed already in Sects. 3.3 and 3.4). Therefore, we added to the simulated model a cutout of noise from a random source free position the measured BB335B 6 cm image.

The set of 1000 simulated sources were now fitted in exactly the same way as the observed images, i.e. as described in appendix B. This includes the threshold, so that if the peak brightness was below the detection threshold in BB335B, the source was not fitted.

We stress that the purpose of these simulations was to investigate the reliability of the fitting method employed here when trying to recover source luminosities and sizes from the observed data. Given the significant uncertainties involved in the setup described above, e.g. on the absolute scaling of the luminosity scale, it is not meaningful to, for example, compare the number of detected sources with the number of observed sources. Future deeper observations together with more detailed models for high-density environments may reduce the uncertainties enough for such comparisons to be of interest.

Appendix D.1: Simulation results

The simulated LD-relation can be seen in Fig. D.1, together with various plots to illustrate the differences between the true simulated luminosities and diameters, and the measured values. Of the 1000 sources simulated, only 55 were found above the detection threshold. This shows the significant impact of a range of explosion energies combined with limited surface brightness sensitivity. As we are likely seeing the brightest sources in any underlying distribution, it is very plausible that the actual number of sources in Arp 220 below our detection limit is indeed a few thousand, as expected from the total supernova rate.

Another interesting result is that the weaker sources are fitted with both too large and too small sizes, illustrating the uncertainties described briefly in Sect. 3.4. While the input distribution of the 1000 sources had more sources at larger sizes, panel (d), the distribution of the sources bright enough to be fitted is almost flat, panel (e). Then, the noise makes the fitting uncertain for

weak sources, panel (f). The final size distribution is very similar to the observed distribution for the weaker sources; note that in this simple simulation we have not added the very luminous SNe. Although this model is based on many assumptions, such as constant density, the qualitative agreement between the model and the results is good enough to argue that size uncertainties are likely present in the observed data.

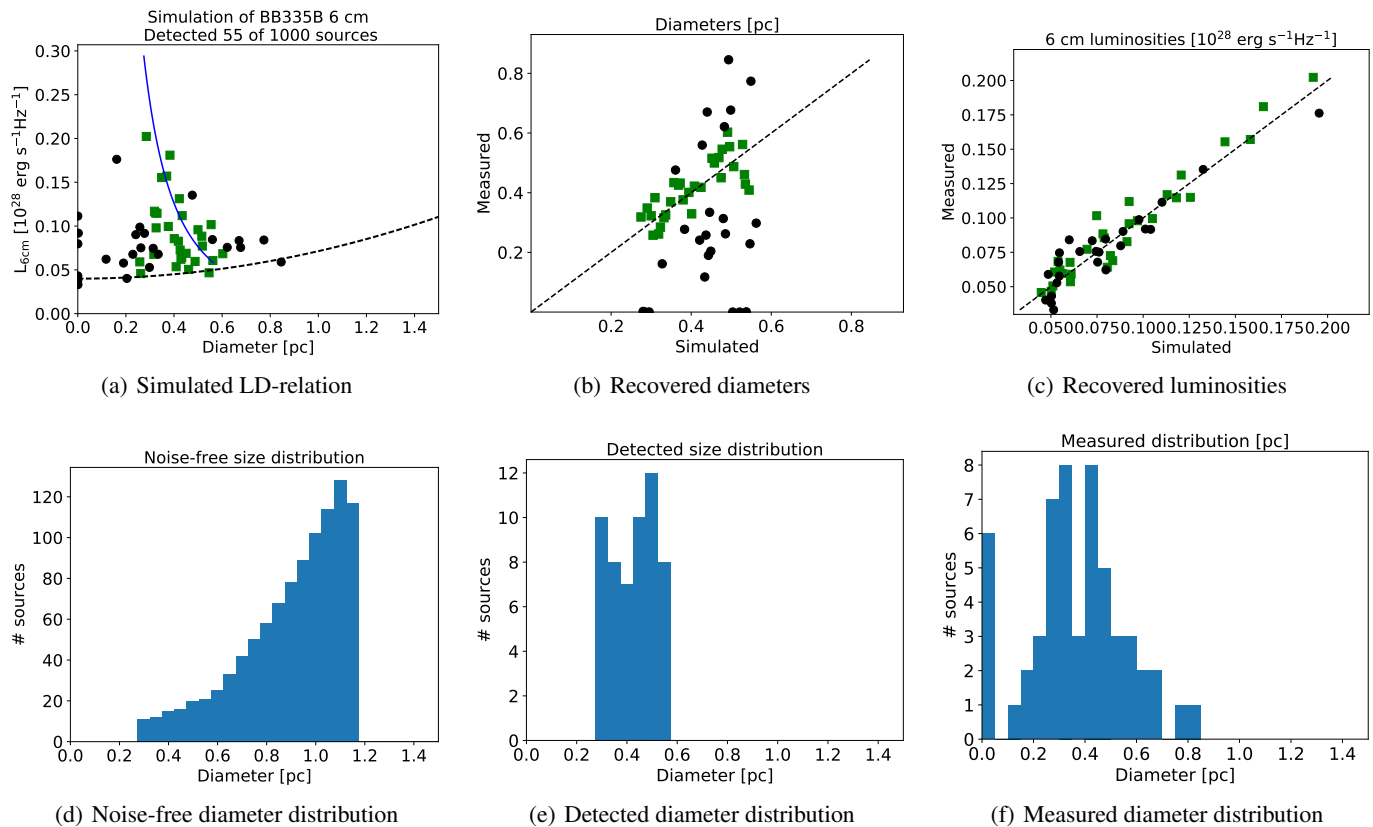


Fig. D.1. Results of a Monte-Carlos simulation of an observed SNR population made in order to calculate uncertainties in size and luminosity estimates (see Appendix D). Panel (a) shows the measured luminosities vs measured diameters for the 55 detected sources, simulated as described in appendix D, where the dashed black line is the surface brightness detection limit. Black circles represent simulated sources where the measured size deviates more than 25% from true size. The green squares represent sources where the measured size deviates less than 25% from true size, i.e. the diameters of these sources are relatively well recovered. Panel (b) shows the measured sizes vs the simulated model sizes. This clearly shows the uncertainty on size measurements for larger, weaker sources. Panel (c) show the measured luminosities vs the simulated model luminosities, with the same colours and symbols as in panels (a) and (b). The dashed lines in panels (b) and (c) represent no difference between the simulated and measured values. We note that although sizes may vary considerably for relatively weak sources, the flux densities are well recovered for all sources. Panel (d) show the distribution of simulated model sources, where we see more large sources than small sources, as expected given the modelled deceleration of the SNR shock with increasing size. Panel (e) shows the modelled diameters of the 55 detected sources. We see that the distribution is flatter than in Fig (d), since more larger sources fall below our surface brightness detection limit. Finally, panel (f) shows the measured diameters of the 55 sources. We see that sources appear both larger and smaller, with a few completely unresolved. The bin width in all three histograms is 0.05 pc.

Appendix E: Source summary slides

The 97 summary pages, one per source, are available in the on-line version of this paper. Each page shows the multi-frequency lightcurve, the source spectra taken from data points close in time, and the size measurements made in all epochs with sufficient resolution.